# A Study of Calorimeter for Future e$^+$e$^-$ Linear Collider

## Kouji Ishii

**Master's Thesis,**
Department of Physics, Faculty of Science, Kobe University,
Rokkodai, Nada, Kobe 657, Japan

### Abstract

As a program of R&D for the JLC experiment, we constructed test modules of compensating Pb-scintillator fiber calorimeter for detection of electromagnetic and hadronic showers. Using these test modules we performed a beam test at KEK PS $\pi 2$ beam line. We also tested three types of photon detection devices in strong magnetic field. In this article I report results of these two tests.

# Contents

# 1 Introduction

Towards 21st. century, electron-positron linear colliders with central mass energies in TeV region are being planned. In these projects, a rich physics will be expected and we can study not only the Standard Model but also new physics beyond the Standard Model. JLC is one of these projects. I have participated to this project and studied the calorimeter with other collaborators. The calorimeter is a device to detect total energy of shower particles ( see Appendix A ). It is one of main detector components in collider experiments. In future electron-positron linear collider experiments, it is essential to have a hermetic detector with super energy resolution. From this requirement, the calorimeter must have good energy resolution for both electromagnetic and hadronic shower profiles and it is desirable to be located inside solenoid. One of the solutions to achieve good energy resolution is compensating Pb-scintillator fiber calorimeter ( see Appendix A.3 ). We constructed test modules and made a beam test at the KEK PS $\pi 2$ beam line. We also tested three types of photon detection devices in strong magnetic field in order to read out signals from the calorimeter inside solenoid. In this article I introduce the JLC experiments and report results of these two tests.

# 2 JLC Experiment

In the JLC-I ( Japan Linear Collider phase 1 ) report [1] published in 1992, it has been proposed to construct the linear collider of center mass energy 300-500 GeV as early as possible. In this section I briefly introduce physics motivations of JLC-I and a detector proposed for the experiment.

## 2.1 Physics

At this energy region following particles, if they exist, can be detected and studied in detail.

- top quark ( $e^+e^- \to Z^0/\gamma \to t\bar{t}$ )

- a ( light ) neutral Higgs boson ( $e^+e^- \to Z^0 h^0$ )

- other neutral Higgs bosons ( $e^+e^- \to Z^0 H^0$ or $H^0 A^0$ or $h^0 A^0$ )

- charged Higgs bosons ( $e^+e^- \to H^+ H^-$ )

- supersymmetric particles ( $e^+e^- \to \tilde{\chi}^+ \tilde{\chi}^-$ or $\tilde{l}^+ \tilde{l}^-$ )

The inside of the bracket is a dominant production at the JLC-I experiment. For neutral Higgs bosons, $h^0$ means a particle expected from the Standard Model or the extension of it and $H^0, A^0, H^+$, and $H^-$ mean the particles coming out from the model of Minimal Supersymmetric extension of the Standard Model. The $\tilde{\chi}^\pm$ and $\tilde{l}^\pm$ are the chargino and slepton particle. The detail is mentioned in later section. Through the search and study of the above particles, we can test the Standard Model with super precision and may be able to test supersymmetry ( SUSY ).

Even if the light neutral Higgs boson can not be detected at the JLC-I experiment, we can get the Higgs mass bound through the radiative correction with super precision measurement of the $m_W$ and $m_t$ ( $\Delta m_t < 1 GeV$ and $\Delta m_W < 20 MeV$ ) due to superior luminosity ( $L = 5 \times 10^{33} cm^{-2} sec^{-1}$ ). The absence of the light Higgs boson implies the death of low energy SUSY and GUT. In this case, we might be able to suggest a new physics through the measurements of anomalous couplings in self-interactions of vector bosons ( $W$, $Z$ and $\gamma$ ). These studies will also open up the possibility to get insights into physics at higher energy scale.

Besides, we can study CP violation and flavor mixing through investigating $B$ physics on the $Z$ pole. The studies of CP violation and flavor mixing are not only to test the Standard Model but also very important to probe underlying physics at very high energies. Due to some superior performances of JLC accelerator ( high luminosity, highly polarized electron beam, and narrow beam ) and large production cross section of $B$ mesons on the $Z$ pole, the JLC-I experiment has some advantages in comparison to the other experiments.

Thus, a large number of physics are expected, we might be able to test physics of the beyond Standard Model. This is the reason for us to look forward to early realization of the JLC-I experiment.

In the next subsections, I give outlines of the physics and show the way of detecting top quarks and Higgs bosons. Both particles are missing in the Standard Model at present, the study of them are main theme of the JLC-I experiment. I also indicate how to detect supersymmetric particles.

Here, I emphasize the detection of these new particles largely depends on the performance of the detector.

The other arguments or details are described in Ref. [1].

### 2.1.1 Top Quark

The top quark must exist and is no heavier than 200 GeV from analyses of the electroweak radiative corrections. ( Ref. [3] )

$$m_W < m_Z \leq m_t \leq 200 GeV$$

In April 1994, the the Collider Detector at Fermilab ( CDF ) group reported the first "evidence" for top quark production at the Fermilab Tevatron collider ( $p\bar{p}$ collisions, $\sqrt{s} = 1.8$ TeV ) in Ref. [4]. They searched for 2-jets and 4-jets events associated with electron or muon. Total 12 events are found with an integrated luminosity of 19.3 pb$^{-1}$. They estimated a top quark mass of $174 \pm 10 \, ^{+13}_{-12}$ GeV/c$^2$ and the $t\bar{t}$ production cross section was measured to be $13.9 \, ^{+6.1}_{-4.8}$ pb. This value of the top quark mass is consistent with the expected value from the electroweak measurement of LEP experiments ( $177 \, ^{+11+18}_{-11-19}$ [1] GeV/c$^2$ Ref. [5] ). But in $p\bar{p}$ collisions, it is too difficult to study detailed features of the top quark, and it will be first performed with e$^+$e$^-$ linear collider in detail.

At JLC-I, we can easily observe $t\bar{t}$ pair production. In that region ( $150 \sim m_t \sim 200$ GeV ) the top quark decays mainly to $bW$. The $W$ boson decays into $q\bar{q}'$ or $l\bar{\nu}$ and the final states of the top quark are classified to the following three cases.

---

[1]The secondary errors are caused by changing the Higgs mass from 60 GeV to 1 TeV.

- 6-jets (45 % )

- 4-jets + 1 charged lepton (44 % )

- 2-jets + 2 charged leptons (11 % )

As an example the first case ( 6-jets ) is considered. In order to select the top quark events from the backgrounds, we applied the following requirements.

- conservation of 4-momentum

- 6-jets at the final states

- two pairs of jets whose reconstructed invariant mass equal to $m_W$

- small thrust ( see Appendix B.1 )

Fig. 1 ( quoted from Ref. [3] ) shows the thrust distributions after the all events selections exclusive of the thrust cut with the Monte Carlo Simulation. It is clear that the thrust cut is efficient for $t\bar{t}$ selection. In this case, a detection efficiency is 26 % and the signal to background ratio exceeds 10.

The top quark we are going to deal with has many unique features, compared to quarks of other flavors. This is primarily due to its large mass and width. The decay of the heavy top quark is dominated by $t \rightarrow bW^+$, and it causes the large width due to the mass difference of W and t ( $m_t \gg m_W$ ). Because of it's large width, the top quark decays before the non-perturbative part of the potential effect it. Thus, the large width prevents this potential from affecting the threshold calculation, uncontrollable theoretical ambiguities are absent from the $t\bar{t}$ system. This implies that we can perform the clear test of perturbative QCD with measurement of the cross section in the whole threshold region ( threshold scan ). Experimentally, the parameters that enter the threshold cross section; $\sigma(\sqrt{s}, m_t, \Gamma_t, \alpha_s(m_Z), m_H, \beta_H$ ) may be determined by the threshold scan. Fig. 2 ( quoted from Ref. [3] ) is an example of the energy scan to determine $m_t$ and $\alpha_s(m_Z)$.

On the other hand, the momentum distribution of the top quark reflects the shape of the $t\bar{t}$ potential that it probes. The momentum distributions provides additional information on $m_t$, $\Gamma_t$, and $\alpha_s(m_Z)$. Fig. 3 ( quoted from Ref. [3] ) is an example of the reconstructed momentum distributions at the $t\bar{t}$ threshold. The measurement of the forward-backward asymmetry is also used with the determination of the $\Gamma_t$ and $\alpha_s(m_Z)$.

Besides, there is another new and remarkable property of a heavy top quark; the heavy top will decay before forming a top-hadron. This enable us to measure the helicities of parent quarks by angular analyses of their decay daughters. The helicity measurement will provide us with a powerful tool to systematically investigate the top quark production and decay vertices, in particular, when the vertices involve new particles expected in the SUSY scenario.

A lot of studies about the top quark are expected in JLC-I. We have to do a intensive tests of the Standard Model through the above precision measurements.

### 2.1.2 Higgs Boson

At the present, the Higgs boson or Higgs mechanism expected from electroweak theory have not been experimentally discovered and lower limit on the mass of the Standard Model Higgs particle is 64.5 GeV at 95 % confidence level ( Ref. [6] ). The Higgs boson does not have a strong confine such as the top quark in the Standard Model framework. But assuming the GUT, Higgs mass does not exceed 200 GeV( Ref. [1]  [2] ), and the light Higgs boson can be searched easily by the process; $e^+e^- \rightarrow Z^0h^0$ at the JLC-I experiment. Especially, a search of intermediate Higgs boson $(m_Z < m_h < 2m_Z)$ is important because it is too difficult to detect such a intermediate Higgs boson at the other experiments. The LEP-II experiment is limited by the center of mass energy and the LHC experiment or other hadron collider do not have a good observable decay mode. On the other hand, the heavy Higgs boson $(2m_Z < m_h)$ will be searched for using the process; $h^0 \rightarrow Z^0Z^0 \rightarrow 4l$ at future hadron colliders ( LHC ).

In the Minimal Supersymmetric extension of the Standard Model( MSSM ), the Higgs sector consists of two doublets, resulting in five physical particles; two CP-even scalars, i.e. a light one ($h^0$) and heavy one ($H^0$), one CP-odd scalar ($A^0$), and a pair of charged Higgs ($H^\pm$). There are relations among the masses of these particles. The $m_{h^0}$, $m_{H^0}$, and $m_{H^\pm}$ can be given in terms of $m_{A^0}$ and $\tan\beta$, where $\tan\beta$ is the ratio of the two vacuum expectation values of two Higgs doublets. The Higgs phenomenology in the MSSM is either the production of only the light Higgs particle with a cross section similar to that of the Standard Model Higgs particle $(m_A \geq 150 GeV)$ or the simultaneous productions of $h^0, H^0, A^0$, and $H^\pm$ ( $m_A \leq 150$ GeV ). In any case, we can discover at least one Higgs particle at JLC-I if nature is really under the GUT condition.

Owing to the mass contribution of coupling to Higgs boson, the decay branching ratio is dominated by $h^0 \rightarrow b\bar{b}$ in case of $m_{h^0} \leq 140$ GeV, while in case of $m_{h^0} \geq 140$ GeV the $h^0 \rightarrow W^+W^-$ decay mode is dominant. Here, we consider the main decay mode is $b\bar{b}$. Depending on the decay modes of $Z^0$, event topologies of the process $e^+e^- \rightarrow h^0Z^0$ are classified into the next three.

- $Z^0h^0 \rightarrow l^+l^-b\bar{b}$ ($\sim$ 10 % )

- $Z^0h^0 \rightarrow q\bar{q}b\bar{b}$ ($\sim$ 70 % )

- $Z^0h^0 \rightarrow \nu\bar{\nu}b\bar{b}$ ($\sim$ 20 % )

A typical event of each topology is shown in Fig. 4 ( quoted from Ref. [2] ). The signals of Higgs boson will be observed as a peak in the invariant mass distribution of 2-jets, requiring the invariant mass of the rest system ( 2 leptons , 2-jets, and missing of the 4-momentum ) consistent with m$_Z$. The main backgrounds come from the following processes.

- $e^+e^- \rightarrow WW$

- $e^+e^- \rightarrow Z^0Z^0$

- $e^+e^- \rightarrow e\nu W$

The background of $WW$ and $Z^0Z^0$ have a peak at the forward direction in differential cross sections. The $WW$ and $e\nu W$ events do not include $b$-quarks at final states. Thus, to select Higgs bosons we required of events produced in central region with $b$-quarks. Fig. 5 ( quoted from Ref. [2] ) shows the reconstructed $m_h$ at an integrated luminosity of 30 fb$^{-1}$ ( correspond $\sim 100$ days running ).

Once a Higgs particle is discovered, a detailed study should come next. The question to be answered is whether the Higgs sector is that of the Standard Model or not. Precise measurements of the production cross section, the decay width, and the decay branching ratio of $h^0$ will answer this question. Fig. 6 ( quoted from Ref. [2] ) shows the contours of the total width of the MSSM Higgs in the $m_{A^0}$ and tan$\beta$ plane. We can also establish the non-minimality of the Higgs boson by measurement of the total cross section of $e^+e^- \rightarrow Z^0h^0$ ( $\sigma_{Zh}$ ) and the branching ratio ( $Br(h^0 \rightarrow b\bar{b})$ ). We should compare the $\sigma_{Zh} \times Br(h^0 \rightarrow b\bar{b})$ of the measurement with that of the Standard Model. It is shown in Fig. 7 ( quoted from Ref. [2] ). The decay channel of $h^0 \rightarrow \gamma\gamma$ is also interesting. For the Standard Model this branching ratio is $\sim 10^{-3}$, but it can be $\sim 10^{-4}$ or much smaller for large tan$\beta$ and relatively small $m_{A^0}$ in the MSSM. Whether we can achieve this study or not much depends on the performance of the calorimeter. The good energy resolution for $\gamma$ ( electromagnetic shower ) is required because the only calorimeter can detect $\gamma$ directly.

The Higgs studies also provide us a possibility to probe higher energy scale physics through the mass ratio of the bottom quark to the tau lepton. At present, large theoretical error on $m_b$ from $b\bar{b}$ potential prevents us from making a precise test of the GUT predictions. However, if the mass of the Higgs boson is in the region where the main decay mode is $b\bar{b}$, we can make a precise measurement of the $b$-quark mass by measuring the branching ratio for $h^0 \rightarrow \tau\bar{\tau}$. In any models which generate the $b$-quark and $\tau$ lepton masses from the same Higgs doublet, the ratio of the branching fraction for $h^0 \rightarrow b\bar{b}$ and $h^0 \rightarrow \tau\bar{\tau}$ is completely fixed up to the ambiguities in $m_b$ and $\alpha_s$. Fig. 8 ( quoted from Ref. [2] ) shows contours of the branching ratio for $h^0 \rightarrow \tau\bar{\tau}$ in the plane of $m_b$ and $\alpha_s$.

The detection of one or more extra-Higgs bosons; $m_{A^0}$, $m_{H^0}$, and $m_{H^\pm}$ is the direct evidence of the non-minimality of the Higgs sector expected in the SUSY models. The processes of the production were already shown ( $e^+e^- \rightarrow H^0Z^0, H^0A^0, h^0A^0$, and $H^+H^-$ ). The detection of the $H^0Z^0$ process is similar way with the light Higgs boson. A detailed studies of the others are reported in Ref. [1], [2] and [7]. In any case, the detection at the JLC-I is easy.

As we described above, we can perform discovery of the intermediate Higgs boson, if it exist. In this case we may be able to test the SUSY with the precision measurement of the Higgs properties or the direct search for the other Higgs bosons.


### 2.1.3  Supesymmetric Particles

The SUSY predicts the existence of a light neutral Higgs boson whose discovery at JLC is easy, as described in the previous section. However the discovery and study of the lightest neutral Higgs boson alone is not enough to prove the SUSY. It is definitely necessary to discover at least one supersymmetric particle. There are a lot of chances to discover at least one supersymmetric particle.

In the framework of Supergravity models with the conditions of the GUT the following

the parameters; ( $m_0, M_2, \mu, \tan\beta$ ), which determined the mass spectra and the interactions of supersymmetric particles, are involved ( Ref. [8] ). In order to avoid unnecessary complications we will make the following simplifying assumption. The R-parity is exactly conserved which implies that supersymmetric particles can only be pair-produced and the Lightest Supersymmetric Particle ( LSP ) is absolutely stable. And the LSP might be the light neutralino to be consistent with cosmology. We further assume that the supersymmetric particle in question is the lightest charged supersymmetric particle.

Under these assumptions, the lighter chargino or the right-handed slepton will be the first observed supersymmetric particle at the JLC-I. The following decay modes of the chargino and slepton are some observable modes. Dominant decay modes of these particles are listed below.

- $\tilde{\chi}^+ \rightarrow \tilde{\chi}^0 W^+$

- $\tilde{\chi}^+ \rightarrow \nu_l \tilde{\chi}^0 l^+$

- $\tilde{\chi}^+ \rightarrow q\bar{q}\tilde{\chi}^0$

- $\tilde{l}^\pm \rightarrow \tilde{\chi}^0 l^\pm$

- $\tilde{l}^\pm \rightarrow l^\pm \tilde{\chi}^0 \chi^0$

where $\tilde{\chi}^0$ is the lightest neutralino ( in this case LSP ) and $l$ can be any of $e$, $\mu$, and $\tau$.

In any case, we can use a missing transverse momentum or a large acoplanarity ( see Appendix B.2 ). The main backgrounds ( example $e^+e^- \rightarrow W^+W^-$ ) are removed by this acoplanarity cut.Fig. 9 ( quoted from Ref. [2] ) shows an example of the acoplanarity distribution for the 2-jets + 1 lepton ( one chargino decays hadronically and the other decays leptonically ) final states from the lighter chargino pair productions with the Monte Carlo simulation. The energy distributions of the 2-jets systems from the lighter chargino decays and of the muons from smuon are shown in Fig. 10 ( quoted from Ref. [2] ) and Fig. 11 ( quoted from Ref. [2] ), respectively.

These figures explicitly show that we can search for a supersymmetric particle at the JLC-I experiment. In order to detect the missing $P_t$, we require a good angular coverage and we must construct the hermetic calorimeter.

## 2.2 Detector

In order to achieve the physics goals of the JLC-I experiments, we need a hermetic detector with super energy/momentum resolution, good b-tagging capability and good lepton identification capability. We made a conceptional design of the detector taking account of the physics simulations as well as the experience of previous experiments and R&D programs. An apparatus proposed by the JLC working group is shown in Fig. 13( quoted from Ref. [1] ). The detector is based on modest extensions of the presently available technology. The parameters and the performances of each detector component are summarized in Table 1( quoted from Ref. [1] ). These values were assumed in the previous physics simulations. Except muon detector ( MUON ), three detectors; namely vertex ( VTX ), central drift chamber ( CDC ), and calorimeter ( CAL ) are placed inside 2 Tesla superconducting solenoid to achieve a hermetic structure and good energy resolution.

| DETECTOR | TYPE | CONFIGURATION | PERFORMANCE |
|---|---|---|---|
| **VTX**<br>( Vertex Detector ) | Silicon CCD | Pixel Size ; 25 μm<br>Number of Layers ; 2 layers<br>Layer Position ; r=2.5cm & 7.5cm<br>Thickness ; 500 μm / layer<br>$\mid \cos\theta \mid < 0.95$ | Position Resolution ; $\sigma = 7.2$ μm<br>Impact Parameter Resolution δ [μm];<br>$\delta^2 = 11.4^2 + (28.8/p)^2 / \sin^3\theta$ |
| **CDC**<br>( Central Drift Chamber ) | Small-cell Jet Chamber | Radius ; r = 0.3 - 2.3 m<br>Length ; l = 4.6 m<br>Number of Sampling = 100<br>$\mid \cos\theta \mid < 0.70$ ( full sampling )<br>$\mid \cos\theta \mid < 0.95$ ( 20 samplings ) | Position Resolution ;<br>$\sigma_x = 100$ μm ( / axial wire )<br>$\sigma_z = 2$ mm ( / stereo wire )<br>Momentum Resolution ;<br>$\sigma_{Pt} / Pt = 1.1 \times 10^{-4} Pt \oplus 0.1\%$<br>$\sigma_{Pt} / Pt = 5 \times 10^{-5} Pt \oplus 0.1\%$<br>( with vertex constraint ) |
| **CAL** | Lead + Plastic Scintillator Sandwitch<br>( Compensated ) | EM part ; thickness = 29 Xo<br>    cell size = 10cm x 10cm<br>HAD part ; thickness = 5.6 λo<br>    cell size = 20cm x 20cm<br>Si Pad ; pad size = 1cm x 1cm<br>$\mid \cos\theta \mid < 0.99$ | Energy Resolution ;<br>$\sigma_E / \sqrt{E} = 15\% / \sqrt{E} \oplus 1\%$ ( e & γ )<br>$\sigma_E / \sqrt{E} = 40\% / \sqrt{E} \oplus 2\%$ (hadron)<br>Si Pad Position Resolution ; $\sigma = 3$ mm<br>Si Pad e/π Rejection = 1/50 |
| **MUON** | Single Cell Drift Chamber | Number of Superlayers ; 6<br>$\mid \cos\theta \mid < 0.99$ | Position Resolution ; $\sigma = 500$ μm<br>Pt > 3.5 GeV ( barrel ) |

\* All momentum and energy are expressed in   [ GeV ].

Table 1: *Parameters and performances of the JLC detector. ( This table is quoted from Ref.[1]. )*

## 2.3   Calorimeter

The following items show the requirements of the calorimeter at the JLC-I.

**1**   good energy resolution for electromagnetic shower: $\sigma_E / E = 15\% / \sqrt{E} + 1\%$

**2**   good energy resolution for hadronic shower: $\sigma_E / E = 40\% / \sqrt{E} + 2\%$

**3**   good position resolution for electromagnetic shower: $\sigma_E / E = $ several mm$/ \sqrt{E}$

**4**   good identification of electrons from hadron backgrounds: a pion rejection factor of about 50 for an electron efficiency of 90 % (the pion rejection factor is defined in section 3.3.4)

**5**   hermetic calorimeter

where energy E is given in GeV. The values are expected to be achieved by a modest extension of current technology. We can detect the high energy neutral particles such as $K_L^0$s, γs and neutrons ( $n$ ) only by the calorimeter. $\pi^0$s decay into two γs immediately after these production.

  γ is important in the case of studying $h^0 \rightarrow 2\gamma$s ( see section 2.1.2 ). This branching ratio is $\sim 10^{-3}$ even if the Standard Model. The mass of Higgs boson from two γs is described as

$$m_h^2 = m_{\gamma\gamma}^2 = 2E_1 E_2 (1 - cos\theta).$$

9

Therefore, the performance of the energy and position resolution for electromagnetic shower is a main key of that study. The process of $Z^0 h^0 \to e^+ e^- b\bar{b}$ also need good energy and position resolution for electromagnetic showers. Because $e^\pm$ radiates $\gamma$ by bremsstrahlung in the CDC, the recoil mass of the $Z$ is depending on the resolution.

A ( hadron ) jet contains about 20 % neutral hadrons ( $K_L^0$, $n$ ). In order to calculate invariant mass of two or several jets, we also need good energy resolution for hadronic shower. As an example, we show Higgs mass resolution in the the $e^+ e^- \to Z^0 h^0$ process. In Fig. 12 ( quoted from Ref. [1] ), the result of a simulation of the di-jet mass resolution, assuming the performances listed in Table 1 and smeared according to the resolution, is presented. The value of $\sigma = 4$ GeV is reasonably good jet mass resolution and it shows a great capability to separate reconstructed Higgs bosons from the backgrounds ( mainly Z particles in the $e^+ e^- \to Z^0 Z^0$ process ) at a few GeV level.

The electron identification is important in many cases. An example is to search for events of $Z^0 h^0 \to e^+ e^- b\bar{b}$ or of top quark associated with the electron. The reason for necessity of hermetic calorimeter is to measured missing energy. In chargino or slepton pair production, a LSP is emitted and carries non-negligible energy, resulting missing energy.

In the Table 1, we chose a compensating Pb-scintillator calorimeter ( sandwich type ) which is one of the solutions. Combination of Pb and scintillator has the potential for compensating calorimeter, which has good energy resolution for hadronic shower ( see Appendix A.3 ). By the calculations of R. Wigmans [10], our requirement for hadronic showers ( $40\%/\sqrt{E}$ ) can be achieved with the configuration of Pb=10mm and scintillator=2.5mm. For electromagnetic showers, it is able to achieve our requirement( $15\%/\sqrt{E}$ ) with the configuration of Pb=4mm and scintillator=1mm by the simulation studies of Y. Fujii in Ref. [11]. Experimentally, ZEUS groups [12] have reported the performance of the compensating Pb-scintillator calorimeter. These studies and results are summarized in Appendix C.1.

On the other hand, the compensating Pb-scintillator fiber calorimeter is one of the other solutions and it has some advantageous performances compared with sandwich type. It is described in next section.

# 3   Tests of Prototype Calorimeter

[2] To achieve the energy resolution of JLC calorimeter we choose compensating Pb-scintillator fiber calorimeter. Because of the fine sampling frequency, fiber calorimeter has better energy resolution than other Pb-scintillator calorimeters such as sandwich calorimeter made of Pb plates, scintillator plates, and wave length shifter bars. Moreover, it is possible to reduce dead space, which might be occupied by wave length shifters in case of sandwich type. The better position resolution can be achieved if the read-out cross section is small. Several groups [14] [21] [22] [25] [27] have reported the excellent performance of the Pb-scintillator fiber calorimeter. These performances are summarized in Appendix C.2.

As a program of R&D for the JLC experiments, we constructed test modules of Pb-scintillator fiber calorimeter. We made a beam test of the modules at KEK PS $\pi 2$ beam line to test the

---

[2]The content of this section will be submitted as a paper.

following items.

- energy resolution for electrons and pions

- signal ratio of electrons to pions(compensation)

- linearity of the signal

- position resolution for electrons

- identification of electrons from pions

- angular dependence of both energy and position resolution for electrons

The angular dependence of both energy and position resolution for electrons is due to lateral shower spread. For Pb-scintillator fiber calorimeter, the beam direction is almost parallel to the fiber direction. Because the electron shower spreads only a few cm and ratio of active layer to absorber in the shower is fluctuated by incident position and angle. Thus, both energy and position resolution depend on the angle and at the small angle ( $\theta_x = 0°$ ) the resolution may be worse. Therfore, we test their effects experimentally.

Due to the limit of the beam energy ( 4 GeV ), response of the modules only to low energy particle could be tested.

## 3.1 Test Modules

We constructed test modules of compensating Pb-scintillator fiber calorimeter. The schematic view of the test modules are shown in Fig. 14. The volume ratio of lead to fiber was set at approximately 4:1 in order to achieve the compensation. For structural hardness the Pb plates contained 6% antimony in weight. A Pb-plate was 10 cm wide and 130 cm long 2 mm thick ( $173X_0$ and $6.2\lambda_0$ ; see Appendix A.2 ), and had machined grooves for the fibers on its upper side ( see Fig. 15 ) with 2.2 mm pitch. The fibers were 1 mm $\phi$ and made of polystyrene-based scintillator KURARAY SCSF-38. The polystyrene core and PMMA clad had refractive indices of $n_1 = 1.59$ and $n_2 = 1.49$, respectively. The surfaces of fibers were painted with white reflector in order to increase light yield. The attenuation length of scintillation light was measured to be roughly 300 cm.

The Pb-plates filled with scintillation fibers in their grooves were stacked to form a test module material with dimension of $10 \times 5 \times 130$ $cm^3$. Because of thickness of the reflector, twenty two or three Pb plates were stacked in the height of 5 cm. At rear end the fibers were grouped into two segment and bundled. The edge of each bundle was cut to make a flat surface and polished. The bundle was glued to an acrylic light guide and viewed by a photomultiplier tube ( Hamamatsu R1335 ). At the front end the edges of the fibers were polished and painted with white reflector. A total of eight modules were constructed and sixteen channels were read out. They were arranged to have a cross section of $20 \times 20$ $cm^2$ as shown in Fig 14. All modules were inserted into a box made of 7 mm stainless steel. It was used as support structure and light shielding.

In addition, we constructed a special test module which had a light guide and a photomultipliers at each end. This module was used to study electrons/pions separation from timing properties of signals at both ends.

11

## 3.2    Setup of the Beam Test

Tests of the calorimeter modules were performed at the $\pi 2$ beam line of the KEK-PS. The maximum momentum available was about 4 GeV/c. The electron/pion ratio in the beam was about 1/1000.

Fig 16 is the schematic view of the setup for the beam test. We set two trigger counters ( S1,S2 ) in front of the movable stage where the calorimeter modules were mounted. Each of them was a scintillation counter with a cross section of $5 \times 5$ cm$^2$, and the distance between the two counters was about 280 cm. There were two gas Čerenkov counters ( C1,C2 ) between the trigger counters to identify electrons and pions. To take electron data the coincidence of S1,S2,C1 and C2 signals were required, while only the coincidence of S1,S2 signals were required for pion data. The electron contamination in the pion data were later removed in the offline analysis.

In order to precisely measure the incident position of the particles, we set two drift chambers ( DC1,DC2 ) between S2 counter and the movable stage. Each of them had readouts for vertical and horizontal position, respectively. The cross section of the drift chambers were $20 \times 20$ cm$^2$, and the position resolution was about 2 mm at the front surface of the test modules.

In addition to the test modules, following detectors were mounted on the movable stage.

- The leakage shower counters which surrounded the test modules (see Fig 17). The counters were sandwich-type calorimeter consisting of scintillator plate ( 2.5 mm thick ) and lead plates ( 10 mm thick ), compensating too. The scintillation light was lead into two photomultipliers through two wave length shifter plate of 2 mm thickness. The active volume of a module was $38.5 \times 18.6 \times 100$ cm$^3$ in size.

- The preshower detector in front of test modules ( upper stream ). The preshower detector consisted of six layers of a scintillator plate ( 1 mm thick ) and a lead plate ( 4 mm thick ), resulting in 4 $X_0$. These preshower detector were also compensating. The scintillation light was lead into four photomultipliers through two wave length shifter plates of 4 mm thickness.

- The silicon-pad detector between the preshower detector and the test modules. The silicon-pad detector consisted of 216 pads ( PIN silicon diodes made in HAMAMATU ), one pad was 300 $\mu$m thickness and $10 \times 15$ mm$^2$ in size, total active area was $18 \times 18$ cm$^2$. This detector was set to test the position resolution for electrons and the separation of electrons from pions through the preshower detector. In this paper we did not use the data of the silicon-pad detector.

All the detectors, namely the test modules, the leakage shower counters, the silicon-pad detector and the preshower detecter, were mounted on a movable stage. The stage could move horizontally and vertically, as well as rotate in the horizontal plane so that the incident angle of the beam to the test modules could be changed.

All the signal from the calorimeters were fed into 12 bit ADCs. The ADC channels had two different ranges to have an effective dynamic range of 15 bit. The signals of the drift chambers were fed into 15 bit TDCs ( same bit type as the ADC ) where one bit corresponded to 100 ps. Once an event was triggered, all the data were taken by a personal computer ( NEC PC98NSR ).

In special runs to take the pulse shape, the signals from the calorimeters were fed into a digital oscilloscope of 2 GHz sampling. The data were transferred to the personal computer.

We took various data changing the setup of the beams and the detectors. The momentum of the beam was set of 1.0 , 1.5 , 2.5 and 4.0 GeV/c. The incident position and angle to the test modules were changed with the movable stage. The data without the preshower detector were also taken.

## 3.3   Analysis

In the following analysis, only single-track events were used. They were selected with the conditions given below.

- The pulse height of each trigger counter ( S1 and S2 ) is consistent with that of a signal minimum ionizing particle. Fig. 18 shows typical pulse height distributions of the trigger counters.

- There was one and only one hit in each drift chamber ( DC1 and DC2 ).

The gain of each channel in the test modules was calibrated with using the electron data to the central region ( $2 \times 2$ cm$^2$ ) of each segments with an incident angle of $3°$ in the horizontal plane ( $\theta_x = 3°$ ). By D. Acosta, *et al.* ( Ref. [14]), the angular dependence of the energy resolution is flat at $\theta_x > 3°$. The electron energies were 1.0, 1.5, 2.5, and 4.0 GeV. The response was found to be linear in the relevant energy range. The leakage shower counters were calibrated in a similar way. The energy resolution of the leakage shower counters for electrons was found to be $\sigma_E/E = 24.0\%/\sqrt{E} + 0.4\%$.

The results were compared with Monte Carlo simulation based on GEANT3. The detail is described in Ref. [9].

### 3.3.1   Energy Resolution for Electrons

To evaluate the energy resolution for electrons we use only the events where electrons hit the center ( $2 \times 2$ cm$^2$ ) of each segments. The total energy of the test modules ( $E_{LEAD/SCIFI}$ ) was calculated as the sum of the signals of all the 16 channels. In case the preshower detector ( PSD ) was located in front, the total energy ( $E$ ) is calculated with the following formula

$$E = \alpha \times E_{PSD} + E_{LEAD/SCIFI}$$

where $E_{PSD}$ is the energy deposit measured in the preshower detector. The coefficient $\alpha$ was determined at each energy point to obtain the best energy resolution. For the data without the preshower detector, $E_{LEAD/SCIFI}$ is simply used as the total energy. An example of the total energy distribution is shown in Fig. 19.

By fitting the total energy distribution to a Gaussian function, we obtained the energy resolution. The results at $\theta_x = 3°$ with and without the preshower detector are given in Table 2 and also shown in Fig. 20. The resolutions can be expressed by the following formula.

$$\frac{\sigma}{E} = \frac{14.4 \pm 1.63\%}{\sqrt{E(GeV)}} + 0.15 \pm 1.03\% \quad \text{with PSD}$$

$$= \frac{15.2 \pm 1.37\%}{\sqrt{E(GeV)}} - 0.58 \pm 0.82\% \quad \text{without PSD.}$$

| Energy | 1 GeV | 1.5 GeV | 2.5 GeV | 4 GeV |
|---|---|---|---|---|
| w/ PSD | $13.8 \pm 0.87$ | $12.6 \pm 0.76$ | $9.45 \pm 0.50$ | $7.23 \pm 0.35$ |
| w/o PSD | $13.4 \pm 0.78$ | $12.5 \pm 0.75$ | $9.53 \pm 0.31$ | $6.81 \pm 0.24$ |

Table 2: *Energy resolution $\sigma/E$ (%) for various energy.*

The angular dependence of the energy resolution was studied with 2.5 GeV electrons at $\theta_x = 0°, 1°, 2°, 3°, 6°$ and $9°$. Fig. 21 shows the results of the energy resolution as a function of the incident angle $\theta_x$. Although the angular dependence is not seen clearly, we observed slightly worse energy resolution at $\theta_x = 0°$. We think a reson for the indistinct angular dependence is due to the low beam energy.

### 3.3.2 Position Resolution for Electrons

The incident position can be obtained from the test modules. The position ( $x, y$ ) weighted by the energy is calculated as

$$x = \frac{\sum_i x_i E_i}{\sum_i E_i}$$

$$y = \frac{\sum_i y_i E_i}{\sum_i E_i}$$

where ( $x_i, y_i$ ) and $E_i$ are the center position and the energy deposit of $i$'the channel. In this analysis the data without the preshower detector is used. Fig. 22 shows the scatter plot of the incident positions measured by the drift chambers and the position derived from the above formula, where the electrons of 4 GeV energy were incident with a horizontal angle ( $\theta_x$ ) of $3°$ to the test modules without the preshower detector in front.

Using these plots and assuming that the positions measured by the drift chambers are correct, we can get functions for further correction. We used the tangential function here. We show the distribution of the difference of the corrected position and the position measured by the drift chambers in Fig. 23. The distributions are fitted to Gaussians, and the resolutions are calculated. The results at $\theta_x = 3°$ are summarized in Table 3 and shown in Fig. 24. The relation between the position resolution and electron energy can be expressed as

14

$$\sigma_x = \frac{6.2 \pm 0.3mm}{\sqrt{E(GeV)}} + 0.6 \pm 0.2mm \quad at\ \theta_x = 3° \ without\ PSD$$

$$\sigma_y = \frac{4.7 \pm 0.3mm}{\sqrt{E(GeV)}} + 1.4 \pm 0.2mm \quad at\ \theta_x = 3° \ without\ PSD$$

The difference of the behaviors between the $x$-coordinate and the $y$-coordinate is considered to be due to the difference of the beam spot at the various beam energy. The position resolution depends on the incident point and at the edge of one segment the test modules have better resolution because we can get more information about the incident point from the adjacent channels.

The angular dependence of the position resolution is studied with the data of 4.0 GeV electrons at $\theta_x = 0°, 3°, 6°$ and $9°$. Fig. 25 shows the results of the energy resolution as a function of the angle $\theta_x$. The angular dependence was not seen.

### 3.3.3 Energy Resolutions for Pions

We use the pion data with incident angle of $0°$ for the energy resolution for pions. The contamination of electrons in the data is removed offline using the information of Čerenkov counters. We calculate the total energy as the sum of all the signals from the test modules and leakage shower counters. Similar to the case for electrons, if the preshower detector was located in front, $\alpha \times E_{PSD}$ is further added to the total energy. An example of the total energy distribution is shown in Fig. 26. The energy resolutions at each energy points are listed in Table 4. They are also shown in Fig. 27.

$$\frac{\sigma}{E} = \frac{31.5 \pm 1.79\%}{\sqrt{E(GeV)}} + 9.06 \pm 1.19\% \ with\ PSD$$

$$\frac{\sigma}{E} = \frac{30.1 \pm 1.82\%}{\sqrt{E(GeV)}} + 7.45 \pm 1.15\% \ without\ PSD.$$

The large constant term reproduced by the simulation [9]. It may be caused by the further shower leakage for pion from the test modules and leakage shower counters. Because of serious problem at high energy, we want to check it experimentally by locating further leakage counters.

| Energy | 1 GeV | 1.5 GeV | 2.5 GeV | 4 GeV |
|--------|-------|---------|---------|-------|
| x | $6.94 \pm 0.13$ | $5.33 \pm 0.12$ | $4.37 \pm 0.10$ | $3.74 \pm 0.09$ |
| y | $6.52 \pm 0.16$ | $4.97 \pm 0.11$ | $4.45 \pm 0.09$ | $4.12 \pm 0.09$ |

Table 3: *Position resolution $\sigma/E$ (mm) for various energy.*

| Energy | 1 GeV | 1.5 GeV | 2.5 GeV | 4 GeV |
|---|---|---|---|---|
| w/ PSD | $40.29 \pm 1.03$ | $35.12 \pm 0.61$ | $28.63 \pm 0.48$ | $24.94 \pm 0.44$ |
| w/o PSD | $37.97 \pm 1.02$ | $31.62 \pm 0.79$ | $26.34 \pm 0.65$ | $22.54 \pm 0.39$ |

Table 4: *Energy resolution $\sigma/E$ (%) for various energy*

The ratio of signal amplitude for electrons to pions are calculated as

$$\frac{e}{h} = \frac{A_e}{A_p} = 1.19$$

where $A_e$ and $A_p$ were coefficients of linear fit in the linearity measurement. In this analysis we didn't take account of the further shower leakage for pions from the test modules and leakage shower counters. The value of the result ( $e/h = 1.19$ ) suggests that the test modules are not exactly compensating.

### 3.3.4 Electron Identification

We can identify electrons from pions using calorimeters by utilizing the difference in the lateral shower profile of electromagnetic and hadronic showers. The preshower detector can also be used for electron identification. As the response of the preshower detector is almost independent of the lateral shower spread, a combination of the calorimeters and the preshower detector can improve for electron identification.

In addition, we may be able to separate electrons and pions by utilizing the difference in the time structure of electromagnetic and hadronic showers.

**Electron Identification from Lateral Shower Spread**

To characterize the lateral shower spread we defined here two variables . One is the containment value $C$ defined as

$$C = \frac{\sum_i E_i \quad (i \; ; \; Center \; of \; 9 \; Modules)}{\sum_j E_j \quad (j \; ; \; All \; test \; modules \; + \; Sandwich)}$$

The suffix $i$ includes the center segment located at the beam position and its eight neighboring ones, while the suffix $j$ includes all test modules and the leakage shower counters. The other variable is the lateral shower spread $S$ defined as

$$S = \frac{\sum_i D_i^2 E_i}{\sum_i E_i}$$

16

where $D_i$ is the distance from the beam position determined by drift chambers to the center position of each segment. Fig. 28 shows the distributions of $C$ and $S$ for electrons and pions of momentum 2.5 GeV/c.

In the preshower detector the distribution for pion has a peak which corresponds to the response of a single minimum ionizing particle, while the energy deposits for electrons show broad distributions at much higher region. Fig. 29 shows the pulse height distributions in the preshower detector for electrons and pions of momentum 2.5 GeV/c.

The scatter plots of the preshower detector signal and $C$ or $S$ values are shown in Fig. 30 and Fig. 31, respectively. These figures indicate the electron identification with the test modules in combination with the preshower detector.

We get the electron efficiency and the pion rejection factor as the following expressions, respectively.

$$Electron\ efficiency\ :\ \frac{NE_{cut}}{NE_{all}}$$

$$Pion\ rejection\ factor\ :\ \frac{NP_{all}}{NP_{cut}}$$

$NE_{all}$ was a number of single-track events selected by DC and $NE_{cut}$ was a number of electron events selected by the calorimeter or PSD, where we used electron data. $NP_{all}$ and $NP_{cut}$ are same definition, where we used pion one. To compare the above analysis by pion rejection factor with fixed electron efficiency, various cuts apply to the data. They are summarized in Table 5. Although the energy is low, results are good. Especially, the test modules in combination with the preshower detector have good capability to the electron identification. ( At the 98% electron efficiency the pion rejection factor already exceeds 50. )

| Electron efficiency | 90 % | 95 % | 98 % |
|---|---|---|---|
| PSD | 10.5 | 9.56 | 7.77 |
| C value | 21.4 | 14.1 | 7.49 |
| S value | 24.7 | 15.5 | 9.78 |
| PSD + C | 94.3 | 74.1 | 50.6 |
| PSD + S | 94.3 | 79.8 | 61.0 |

Table 5: *Pion rejection factor for various technique.*

**Electron Identification from Time Structure**

Electromagnetic or hadronic showers have different timing time characteristics. The differences between electron and pion signals came from the following characteristics.

1. The longitudinal shower spread. As the typical hadronic showers spread over a larger area than electromagnetic showers, the hadronic showers result in broader signals ( large pulse widths ).

2. The neutron component in hadronic showers. This effect appears in tail of the signals.

3. The longitudinal depth at shower maximum.[3] The shallow shower maximums of electrons cause the large and definite timing difference of the signals at both ends.

We have investigated two methods, one is a pulse width to characterize the above first and second items, and the other is the timing difference to characterize the above third one. We used both the tests modules and the special test module ( having a read out device at each end, see section 3.1 ). In the special runs ( see section 3.2 ) the signal were fed to the digital oscilloscope, the information of the time structure of showers were extracted. For the tests modules we have investigated a pulse width of the signals to characterize the pulse shape. On the other hands, for the special module we have investigated the time difference of the signals at both ends, added to the pulse width. The time difference with the special module is a new technique, have a capability of separating electrons and pions as well as pulse shape.

In this analysis the pulse widths were defined as fall time from 90 % peak to 40 % peak with and from 95% peak to 45 % peak with the special test module in order to obtain the best separation of electrons from pions. Fig. 32 and 33 show the distributions of the pulse widths for electrons and pions of momentum 4 GeV/c with the test module and the special test module, respectively. The incident position to the test modules was the center of the segment and the incident angle was $3°$ in the horizontal plane. On the other hand, in case of the special test module the incident position was changed to the edge and the incident angle was also changed to $6°$ to avoid the beam hitting the light guide and phtomultiplier. Because of this condition the distribution of electrons with the special test module was broader than that with test modules and therefore the pion rejection factor with the special test module was worse. The electron efficiency and the pion rejection factor are summarized in Table 6 and 7.

| Electron efficiency | 93.6% | 97.0% | 98.3% |
|---|---|---|---|
| PWD | 6.92 | 4.10 | 3.65 |

Table 6: *Pion rejection factor with the test module. The PWD shows the method of the pulse widths.*

The distributions of the timing difference of the signals for electrons and pions incident to the special test module are shown in Fig. 34. The energy, incident angle and incident position were 4 GeV, $6°$ and edge of the segment. As the timing difference is almost independent from the

---

[3]By D.Acosta *et al.* [17] some signals for hadronic showers have two peaks coming from the direct light and the light reflected off the front end of the alminized fibers at the high energy ( 40 GeV or larger ). As the deeper shower maximum cause the broader signals, the hadronic showers result in the broader signals. In our test modules the front end of the fibers were polished and painted with white reflector, and this effect wasn't seen at the low energy.

pulse width we can use them in combination. The scatter plot of them are shown in Fig. 35. The electrons efficiency and pions rejection factor are also collected in Table 7.

By D.Acosta *et al.* [17] the time structure has high sensitivity of the separation electrons from pions. They reported the pion rejection factor is measured to exceed 1000 at the energy of 80 GeV by the analysis of the pulse width. On the other hand, the other group [15] report that no separation was possible by timing discrimination at the low energy ( below 10 GeV ). They explained that their calorimeter was too short to detect it. Their calorimeter is only 1.32 interaction length. It will be impossible to measure the total energy for the pions with their detector, and thus, it is almost impossible to detect the longitudinal shower spread and the neutron component by the pulse width analysis. Our results show the possibility of the separation, though it is a little. The reason of the low sensitivity of the separation will be due to the low beam energy.

| Electron efficiency | 90 % | 95 % | 98 % |
|---|---|---|---|
| PWD | 2.95 | 2.29 | 1.91 |
| TD | 2.85 | 2.53 | 2.17 |
| PWD + TD | 6.90 | 4.85 | 3.20 |

Table 7: *Pion rejection factor with the special test module. The PWD shows the method of the pulse widths and TD shows the method of the timing difference.*

## 3.4   Discussion

In this section, we describe the finding for the studies of the compensating Pb-scintillator fiber calorimeter through the construction and the beam test. We also discuss further studies to be done.

**Performances**

From the above results of analysis, we found the following performances of the compensating Pb-scintillator fiber calorimeter.

- They have best energy resolution for both electromagnetic and hadronic showers in the one body types at the present.

- They also have good position resolution for electromagnetic showers.

- There is room for argument on the $e/h$. If the compensation is complete, the energy resolution for hadronic showers are further good.

- In the combination with the PSD, the calorimeter have good capability to the electron identification from lateral shower spread. But due to the low energy, the electron identification from time structure is not clear.

19

As a whole, we can find the good performances of that calorimeter.

**Technical Difficulties in Constructing**

But through constructing of our test modules, we found several technical difficulties; a large number of handling fibers, making grooves, control painting technic, and so on. The following items are some problems of our constructing when the mass production is considered.

- In order to increase the light yield, we polished the both fiber edges. We expended a great deal of time in doing the work, it may be possible only to cut with diamond cutter.

- We used grooved Pb plates, it was simple but too many process was needed. Many processes increase large cost. The construction of the collider experiments usually needs a huge cost and it is serious problem to come expensive. We should suppress the cost as low as possible.

- Moreover, using the Pb plates become difficult to support it, when we set up it in the barrel region. It is desirable to use PB blocks, if it's possible.

- Painting is a problem, too. Painting made space between lead plates, non-uniformity of the module height. Indeed, one test module of 5 cm in height made of only 22 or 23 Pb plates of 2 mm and the center of the test module was fallen in a few mm. Because of these effects the dead space increases, the uniformity may be worse, and the energy and position resolution might be worse.

Up to the present, we have not found a best way yet.

**Further Studies**

On the other hand, a lot of tasks are remained. We describe the further studies to be done in future.

- We must perform the tests with the test modules at the high energy. For the center of mass energy will be designed as 300-500 GeV, the beam energy of tests of the calorimeter needs at least a hundred GeV.

- The simulation studies are also important tasks. We will have to define the parameters of the calorimeter, exactly. There are many parameters for the Pb-scintillator fiber calorimeter ( diameter of fibers, volume ratio of Pb to fibers, cross section of a read out channel, and so on ), and each parameter have much influence on the performance of the calorimeter. To define parameters is mainly investigated by the simulation.

- The long term stability is also important in a long standing experiments, such as JLC. For the fiber calorimeter, the response of scintillating fiber is changed or down. Because the energy resolution is direct depending on the number of photons ( light yield ), the low response will cause the worse energy resolution.

- The study of necessity of the preshower detector is remained. The preshower detector located in front of fiber calorimeter may reduce the dependence of incident position ( see section 3 ). This subject is also associated with the development of the photon detectors operational with strong magnetic field ( see next section ).

# 4   Tests of Photon Detection Devices

[4] Because of thinking to locate the calorimeter to inside the solenoid, we need to develop a high sensitivity photon detectors operational with strong magnetic field. The hadronic calorimeters are usually made with sampling configuration and their output photons are not enough to read out with PIN silicon photodiodes. In case the preshower detectors have to read out, their output photons are also not enough. The required value is $10^5$ order of gain under the magnetic field of 2.0 Tesla.

In this report we present results of the tests of three types of photon detection devices in strong magnetic field ; a fine-mesh photomultiplier ( FMPMT ), a hybrid photodiode ( HPD ), and a vacuum avalanche photodiode ( VAPD ). Strong magnetic field upto 2.5 Tesla were applied for FMPMT and HPD, and upto 1.0 Tesla for VAPD.

## 4.1   Photon Detection Devices

A schematic view of the FMPMT is shown in Fig. 36. An incoming photon is converted on the photocathode into a photoelectron, then accelerated by the electrostatic field, hit the fine-mesh, and product some secondary electrons. Similar to photomultipliers the acceleration and production were repeated in pairs and a large number of the electrons is gathered and produces the output current at the last dynode. It is well known that the FMPMT is operational in magnetic fields less than $\sim 1$ Tesla [29]. However for future collider experiments, much higher magnetic field is expected. In this test we used a Hamamatu H2611SXA(24) FMPMT [30]. This is one of test pieces aimed at very high gain by increasing number of dynodes upto 24 stages. Parameters of the H2611SXA(24) are listed in Table 8.

HPD is a new photon detector developed by DEP in collaboration with Canberra, INFN and CERN-LAA project [31] [32]. A basic configuration of the HPD is shown in Fig. 37. The same as FMPMT, an incoming photon is converted on the photocathode into a photoelectron, accelerated by the electrostatic field toward the PIN silicon photodiode. The accelerated photoelectrons stop in the depletion volume by generating electron-hole pairs. The gain is proportional to the phtoelectron accelerating voltage. The collection of this charge produces the output current pulses of the HPD. We tested commercially available HPD PP350B [33]. Parameters of the PP350B are listed in Table 8. Since detailed study was already reported in reference [32] for prototype HPD, we somewhat concentrate here on the results with magnetic field of 2.0 Tesla and 2.5 Tesla.

VAPD is a hybrid photon device similar to HPD, using a large-area avalanche photodiode ( APD ) [34] instead of a PIN silicon photodiode as the photoelectron detector [35]. Fig. 38 shows

---

[4]The content of this section will be submitted as a paper.

a schematic view of the VAPD. As a first step the accelerated photoelectrons by the electrostatic field generate a lot of electron-hole pairs in the APD. In the APD by the usual avalanche process one electron-hole pair generates many electron-hole pairs as a second step, the VAPD results in having much higher gain than the HPD. Several test results without magnetic field were reported in references [36]. Here we report its performance in magnetic field upto 1 Tesla. Though the setup for VAPD was the same as that for the other two devices, we could not apply magnetic field more than 1 Tesla due to some magnetic material inside the VAPD. Parameters of the VAPD are also shown in Table 8.

| Parameters | FMPMT | HPMT | VAPD |
|---|---|---|---|
| Photo-cathode | 36 mm | 25 mm | 18 mm |
| Dynode diameter | 36 mm | - | - |
| Anode/Si diameter | 36 mm | 25 mm | 16 mm |
| PC-Anode/Si diameter | 19 mm | 5.6 mm | ( 6 mm max )[*3] |
| max PC voltage | -2.7 kV | -8.0 kV | -15.0 kV |
| max bias voltage | - | 75 V | 2250 V |
| Gain w/o magnetic field | $1.2 \times 10^{8[*1]}$ | 1600 | $1.0 \times 10^5$ |
| Quantum efficiency | 20 % ( 420 nm ) | 20 % ( 480 nm ) | 23 % ( 450 nm ) |
| Rise time | 2.1 ns[*2] | 8 ns | 9 ns |

Table 8: *Parameters of the FMPMT, HPD, and VAPD taken from technical data. (\*1) Gain at -2.0 kV. (\*2) Rise time of commercial tube R2450-09. (\*3) This distance is not controlled at fabrication process.*

## 4.2   Setup in Strong Magnetic Field

The tests were carried out at the Photon Synchrotron Experimental Hall of KEK. Due to the limitation of the availability of magnets, tests were done using two magnets. One was a so-called 8D320 normal conducting bending magnet upto 2.0 Tesla and the other was a so-called SKS superconducting spectrometer magnet [37] upto 3.0 Tesla. Unfortunately the SKS magnet was under quench training, magnetic field only upto 2.5 Tesla was available. The data at 2.0 and 2.5 Tesla were taken with the SKS magnet, while those at 2.0 Tesla and below were taken with 8D320 magnet. Data at 2.0 Tesla taken with the SKS magnet and with the 8D320 magnet show no significant discrepancy. The data at 2.0 Tesla with the 8D320 magnet were taken during both ramping up and ramping down the magnet to check the reproductivity. They agreed to each other very well.

The setup is shown in Fig. 39 schematically. A blue LED of 450 nm [38] was directly mounted above the photocathode of the devices. Distribution of light on the phtocathode was measured without magnetic field using the slits having various diameters. The result is shown in Fig. 40. The LED have some light spread and at the large angle it wasn't neglected because the

photo-electrons are missing the dinode due to the tilted electron trajectory along the magnetic field. In the following sections we take it into account with estimation. Variation of light output of the LED due to the magnetic field was measured to be less than 1.5 % for all measurement conditions ( See Fig. 41 ) and it is neglected in this analysis.

Data are taken with a CAMAC charge sensitive ADC. The same setup was used for all three devices except for the optical filter.

Number of photoelectrons ( $N_{pe}$ ) for the FMPMT was obtained from the width ( $\sigma$ ) of the pulse height distribution;

$$N_{pe} \; = \; \left( \frac{M}{\sigma} \right)^2 ,$$

where $M$ is the mean of the pulse height distributions. For the other devices they were estimated from that for the FMPMT, with the attenuation factor of the optical filter and quantum efficiencies. The gain ( $G$ ) was obtained from the $N_{pe}$ and $M$;

$$G \; = \; \frac{M}{N_{pe}} \; \times \; \frac{0.25 \times 10^{-12}C}{1.6 \times 10^{-19}C} \; .$$

Pulse-to pulse fluctuation of the LED light yield was obtained from the width of the pulse height distribution of HPD. As a large number of photons ( exceed one million photons ) are inputted, photon statistics could be neglected in the HPD measurement. Subtracting the noise contribution from the width, pulse-to-pulse fluctuation was estimated to be 0.7% and negligible.

We also measured the uniformity of the pulse height with FMPMT and HPD without magnetic field after the tests. Results are shown in Fig. 42 and Fig. 43, respectively. As we observed good uniformities with them, these effects are neglected in this analysis.

In the following subsection results of the measurements for each device are presented.

## 4.3   Results

### 4.3.1   FMPMT

We measured the gain of the FMPMT for various magnetic field strength. The tilt angle $\theta$ between the device axis and the magnetic field was set to be 0° and 35°. The results are shown in Fig. 44. The nominal high voltage ( HV ) for the FMPMT was 2.7 kV. However some measurements at low magnetic field were performed with lower HV. The measurements are normalized to the gain at the nominal HV using the known HV-gain relation. Error bars shown in the figure denote the normalization errors. If the magnetic field is parallel to the device axis ( $\theta = 0°$ ), the gain decrease quite rapidly. On the other hand, in the case of $\theta = 35°$, the gain is significantly higher in general, and exceeds $10^5$ even at 2.5 Tesla.

In Fig. 45 the gain is plotted for various tilt angles. The gain changes more steeply as the magnetic field gets stronger and the highest gain is $\theta = 35°$ in every magnetic fields. These can be explained by the loss of electrons and the self-shielding of dynodes [29], both are caused by

the electron trajectly tilted along the magnetic field. The loss of electrons is calculated from the parameters of the configuration in Table 8. The photoelectrons originating at the center of the photocathode start to miss the anode at $\theta = 40°$. On the other hand, the self-shielding effects of dynodes can be explained that some secondary electrons emitted from the upper of a dynode are re-absorbed by the dynode itself. It is $\theta = 35°$ that most electrons can reach the next stage by passing through holes of the mesh.

According to the measurements, the required high gain is easily achieved with the FMPMT in the strong magnetic field, if the device axis can be appropriately set with respect to the magnetic field.

### 4.3.2 HPD

We measured the gain of the HPD in various magnetic field. The gain dependence on the magnetic field strength and on the tilt angle are shown in Fig. 46 and 47, respectively. As is expected, gain reduction was not observed for the magnetic field being parallel to the HPD axis, while a significant gain decrease was observed for $\theta = 60°$.

The gain is reduced in tilted magnetic field because of two reasons; one is the energy loss of photoelectrons in the surface dead layer of the silicon [33], and the other is the shift of the photoelectron image on the silicon. The photoelectrons lose their energies before entering the depletion region in the surface dead layer. For the tilted magnetic field, incident angles of the electrons are no more normal to the silicon because of the cycloid motion, and the energy loss in the surface dead layer increases. Assuming that electric and magnetic fields are uniform inside the HPD, exact orbit equations can be numerically solved. We obtain that the gain is reduced by 17 % for the case of $\theta = 60°$.

The other origin of the gain reduction is the loss of photoelectrons due to the shift of the photoelectron image in the magnetic field. From the measured distribution of the LED light on the photocathode, the loss of photoelectrons is calculated to be 22 % for the case of $\theta = 60°$. The calculation is consistent with the measurement and the behavior of HPD is roughly explained by these effects.

### 4.3.3 VAPD

The VAPD has almost the same structure as the HPD, and is expected to work under strong magnetic fields. In Fig. 48 the gain is plotted for the magnetic field strength up to 1.0 Tesla. In Fig. 49 the gain is plotted for various tilt angles at 0.5 Tesla. For $\theta = 60°$, in contrast with the HPD case, the gain decreases quite rapidly down to $\sim 1/30$ of that without magnetic field.

Assuming that electric and magnetic fields are uniform inside the VAPD, the effect of cycloid motion can be calculated. The gain reduction due to the tilted incident angle is very small because of the high electric field, and is calculated to be only 6 % effect. The effect of the photoelectron image shift is larger due to the small APD diameter, and is calculated to be reduction down to 1/6. However the measured reduction is much bigger than calculations and these effects alone can't explain the behavior of the VAPD.

## 4.4 Discussion

The performance of them are not sufficient in some points for our requirements; a high sensitivity photon detectors operational with strong magnetic field ( $10^5$ order of gain under the magnetic field of 2.0 Tesla ). The FMPMT has a strong dependence of tilt angle ( $\theta$ ), and it is not desirable. The gain of the HPD is too low to use for the hadronic calorimeters or the preshower detectors. But if the gain will be improved in future, it is most capable. The VAPD is too expensive.

# 5   Conclusion

A sampling calorimeter consisting of 1 mm diameter scintillation fibers embedded in Pb had been constructed and tested for electrons and pions of below 4 GeV energy. The volume ratio of Pb to fibers was set at approximately 4:1 in weight in order to achieve the compensation.

The energy resolution for electrons was measured to be $14\%/\sqrt{E(GeV)}$ plus sufficiently small energy independent term with PSD. The position resolution for electrons was measured to be roughly $6mm/\sqrt{E(GeV)}$. The energy resolution for pion was measured to be $30\%/\sqrt{E(GeV)}$ plus 7.5 % constant term. This large constant term was caused by incomplete shower containment. The various ways to discriminate electrons and pions were investigated. Even at the low energy, the separation by using the lateral shower spread was good. Especially, the test modules in combination with the preshower detector have good capability to the electron identification. ( At the 98% electron efficiency the pion rejection factor already exceeds 50. ) But the separation by using the time structure was not good. We obtained only a few pion rejection factor at the 4 GeV energy.

The results are consistent roughly with the results of the other groups experiments [14] $\sim$ [27] and our simulation study. The behavior of the test modules ( contained the special test module ) are well explained. Although at the low energy, the compensating Pb-scintillator fiber calorimeter shows a high performance. These results confirm us that it is a candidate for the JLC calorimeter.

We have also tested three types of photon detection devices in strong magnetic fields. The FMPMT and HPD are found to be operational up to 2.5 Tesla with appropriate field directions, and their behavior is reasonably understood. The test of the VAPD was rather limited in terms of the magnetic field strength, and the behavior under tilted magnetic field is not fully explained yet. However the device is also operational at least in axial magnetic field of 0.5 Tesla.

The development of the photon detection devices are significantly and one of the many problems. The performance of them are not sufficient in some pooints for our requirements ( see section 4.4 ). In future we have to improve them and achieve these requirements.

At last, I hope the early realizing of JLC experiments and I'm looking forward to the new physics at JLC-I.

# Acknowledgment

# APPENDIX

# A    Calorimeter

## A.1    Principle

[5] The calorimeters are an important class of detector used for measuring the energy and position of particle by its absorption. The incident particle will interact with the material, generating secondary particles which will themselves generate further particles, and so on, so that a cascade or shower develops. The shower is predominantly in the longitudinal direction, but will be subject to some transverse spreading due both to multiple Coulomb scattering and transverse momentum of the produced particles. Eventually all, or almost all, of the primary energy is deposited as ionization or excitation in the calorimeter, and gives a signal in the detector part of the devices. A response of the signal is proportional to the number of shower particles or the energy of the incident particle. Thus, the absorption process is statistical, and the fractional energy resolution $\Delta E/E$ varies as $E^{-1/2}$.

There are several reasons why calorimeters are important, especially at high energies;

- they can detect neutral as well as charged particles by detecting the charged secondaries, if the incident particles cause the shower.

- they can achieve a precision energy measurements even at high energies because of the fractional energy resolution $\Delta E/E$ varies as $E^{-1/2}$.

Since the characteristics of electromagnetic and hadronic showers are somewhat different it is convenient to describe each separately.

**Electromagnetic showers**

When a high-energy electron, positron and photon interacts with matter we have seen that the dominant process is due to bremsstrahlung for $e^{\pm}$ and pair production for $\gamma$. Thus the initial particle ( $e^{\pm}$ or $\gamma$ ) will lead to a cascade of $e^{\pm}$ pairs and photons via these two processes, and this will continue until the energies of the secondary electrons fall below the critical energy $E_c$ where ionization losses equal those from bremsstrahlung ( $E_c \sim 600\,\mathrm{MeV/Z}$ ).

In a simple model, each particle ( $e^{\pm}$ or $\gamma$ ) travels one radiation length ( $X_0$; see latter ) and then interacts with the matter by these two processes ( bremsstrahlung or pair production ). If the initial particle has energy $E_0 \gg E_c$, then after $t$ radiation lengths the shower will contain $2^t$ particles with mean energy $E_0/2^t$. The cascade stops approximately when $E_0/2^t = E_c$. Therefore, the number of generations up to the maximum is $t = \ln(E_0/E_c)/\ln 2$, and number of particles at the maximum $N_{max} = 2^t = E_0/E_c$.

The main features of this simple model are observed experimentally, the energy resolution of an electromagnetic calorimeter depends on statistical fluctuations, and it is typically $\Delta E/E \sim 0.05/\sqrt{E}$, where $E$ is measured in GeV.

---

[5]The content of this subsection is quoted from Ref. [39]. A detail is seen in Ref. [40].

**Hadronic showers**

Although hadronic showers are qualitatively similar to electromagnetic ones, shower development is far more complex because many different processes contribute to the inelastic production of secondary hadrons. The scale of the hadronic shower is determined by the nuclear absorption length ( $\lambda_0$; we defined it as nuclear interaction length, see latter ). Since the $\lambda_0$ is larger than $X_0$, hadron calorimeters are thicker devices than electromagnetic ones. Another difference is that some of the contributions to the total absorption may not give rise to an observable signal in detector. An example is a leakage of secondary muons and neutrinos from the calorimeter, and the loss of 'visible' or measured energy for hadrons is typically 20-30 % greater than electrons.

The energy resolution of calorimeters is in general much worse for hadrons than electrons and photons because of the greater fluctuations in the development of the hadron shower. An example is the number of $\pi^0$s produced in the early stages of the cascade. Because the $\pi^0$ decays two $\gamma$s, the shower may develop predominantly as an electromagnetic one. These various features lead to an energy resolution of typically $\Delta E/E \sim 0.5/\sqrt{E}$, where $E$ is measured in GeV.

## A.2 Definition of the $X_0$ and $\lambda_0$

The radiation length ( $X_0$ ) is defined as

$$\frac{1}{X_0} = 4\alpha \frac{N_0}{A} Z(Z+1) \, r_e^2 \, \ln\frac{183}{Z^{1/3}}$$

where $r_e = e^2/mc^2$ is the classical electron radius, $N_0$ is Avogadro's number, $Z$ and $A$ are the atomic number and mass number of the medium, and $\alpha = e^2/4\pi\varepsilon_0\hbar c$ is the electromagnetic fine structure constant.

The energy loss by the bremsstrahlung in traversing a thickness $dx$ of medium ( $(-dE/dx)_{brem}$ ) and the average energy of a beam after traversing a thickness $x$ of medium ( $<E>$ ) will be shown in the next formula with using the radiation length;

$$-\frac{dE}{dx} = \frac{E}{X_0},$$

and

$$<E> = E_0 \exp\left(-\frac{x}{X_0}\right).$$

Because the pair production process is closely related to electron bremsstrahlung, the cross-section is characterized by the radiation length and is given to a good approximation by

$$\sigma_{pair} = \frac{7}{9}\frac{N_0}{A}\frac{1}{X_0}.$$

The beam loss by the pair production in traversing a thickness $dx$ of medium ( $(-dI/dx)_{pair}$ ) and the beam intensity after traversing a thickness $x$ of medium ( $I$ ) will be shown in the next formula;

$$-\frac{dI}{dx} = \frac{I}{\lambda}$$

and

$$I(x) = I_0 \exp\left(-\frac{x}{\lambda}\right)$$

where $I_0$ is initial beam intensity ( $I$ photons ) and $\lambda = (A/N_0\sigma_{pair}) = 7/9 X_0$ is the mean free path of photon by pair production.

On the other hand, the nuclear absorption ( or interaction ) length ( $\lambda_0$ ) is defined by

$$\lambda_0 \equiv \left( \frac{A}{N_0 \sigma_{inel}} \right),$$

which governs the probability of an ineleastic collision.

## A.3  Compensating

A compensating is one way of improvement of the energy resolution for hadronic showers. By Richard Wigmans [10], there are two components of the hadronic showers, one is $\pi^0$ component ( $\pi^0 \rightarrow 2\gamma$; so, electromagnetic component ) and the other is purely hadronic one. If the response ( or 'visible' energy ) of these components is differ, a signal average of electrons is not equal to that of pions ( the signal ratio $e/h \neq 1$ ), and the energy resolution will be not to scale with $E^{-1/2}$ and worse. The signal ratio $e/h = 1$ is a main key of the compensating.

It is well known that the compensating is achieved by using $^{238}$U as absorber. Low-energy neutrons from nuclear breakup cause fission in the uranium, and thus their is converted into charged particle ionization and measured. In Ref. [10], R. Wigmans reports the compensating can also be achieved for lead and even iron calorimeters theoretically. In fact, a variety of absorber/detector combinations can be made compensating, provided that the response to the neutron shower component is adequately amplified with respect to the charged shower components. This may be achieved with hydrogenous active material.

For the combination of Pb and scintillator sampling calorimeter, it was predicted that the compensating can be achieved if the volume ratio of lead to scintillator is set at 4:1. In case of complete compensation, the Monte Carlo simulation suggests that the energy resolution of Pb-scintillator sampling calorimeter ( sandwich type ) for hadronic shower is $\Delta E/E = 40\%/\sqrt{E}$. But in experimental studies, ZEUS test group reported the signal ratio $e/h$ was not exactly equal 1 and resulted in worse energy resolutions [12]. And the signal ratio $e/h$ of the Pb-scintillator fiber calorimeter was also not exactly equal 1 [18]. These resolutions and signal ratios are summarized in Table 9.

| Constitution | EM | HAD | e/h | Group and Ref. |
|---|---|---|---|---|
| Pb10mm/scinti2.5mm(cal) | - | $40\%/\sqrt{E}$ | exactly 1 | R. Wigmans [10] |
| Pb10mm/scinti2.5mm(exp) | $23\%/\sqrt{E}$ | $44\%/\sqrt{E}$ | 1.05 | ZEUS test [12] |
| Pb/scinti=4/1, 1mm$\phi$(exp) | $13\%/\sqrt{E}$ | $30\%/\sqrt{E}$ | 1.15 | SPACAL collab. [18] |

Table 9: *Energy resolutions and signal ratio of e/h for compensating Pb-scintillator calorimeter.*

## A.4 Examples

A calorimeter is classified a homogeneous type and a sampling type. The former is homogenized with absorber and detector ( such as a block of lead glass ), the later is separated the absorber (e.g. a metal such as lead ) and detector ( scintillator, MWPC etc.). An energy resolution of the sampling calorimeter for electromagnetic shower is roughly shown as

$$\frac{\sigma}{E} \;=\; \sqrt{\left(\frac{\sigma}{E}\right)_s^2 + \left(\frac{\sigma}{E}\right)_{N_e}^2}$$

where $(\sigma/E)_s$ is the energy resolution due to sampling fluctuations and $(\sigma/E)_{N_e}$ is the energy resolution due to photoelectron statistics. Thus, the sampling frequency as well as the light yield is important to improve the energy resolution of sampling calorimeter. For the homogeneous calorimeter, the $(\sigma/E)_s$ is absent and the light yield is dominant subject.

On the other hand, according to the detected particles, we can also distinct a electromagnetic shower counters and a hadronic ones. The hadron calorimeters are usually build as sampling types because the large and heavy detectors are need to absorb the all particles of hadronic shower ( $\lambda_0 > X_0$; see APPENDIX A.1:hadronic shower ).

In Ref. [41] and Ref. [42], most of calorimeters are well reviewed. I pick up and show the typical energy resolutions of several types of calorimeters in Table 10.

| Constitution | EM | HAD | Group |
|---|---|---|---|
| Pb glass | $6.3\%/\sqrt{E}$ | - | OPAL |
| CsI | 2% at 1 GeV | - | CLEO |
| BGO | 1.8% at 1 GeV | - | L3 |
| Pb2mm/GAS3.2mm | $18\%/\sqrt{E}$ | - | ALEPH |
| Pb2mm/LqAr2.75mm | $10\%/\sqrt{E}$ | - | SLD |
| Pb3.2mm/Scinti5mm | $13.5\%/\sqrt{E}$ | - | CDF |
| Fe50mm/GAS3.2mm | - | $80\%/\sqrt{E}$ | ALEPH |
| Pb6mm/LqAr2.75mm | - | $45\%/\sqrt{E}$ | SLD |
| Fe25mm/Scinti10mm | - | $80\%/\sqrt{E}$ | CDF |
| U3.2mm/Scinti3mm | $23\%/\sqrt{E}$ | $44\%/\sqrt{E}$ | ZEUS |

Table 10: *Examples of several types of calorimeters.*

# B Algorism

## B.1 Thrust

The $Thrust\ T$ is defined as

$$T \;=\; \max\left[\frac{\sum_i |\vec{p}_i \cdot \vec{n}|}{\sum_i |\vec{p}_i|}\right]$$

where $\vec{p}_i$ is the momentum of the $i$-th particle in an event. The unit vector $\vec{n}$ is called thrust axis and defined at maximized $T$.

## B.2 Acoplanarity

The $Acoplanarity\ A$ is defined as

$$A \;=\; 4\min\left[\frac{\sum_i |\vec{p}_i \cdot \vec{n'}|}{\sum_i |\vec{p}_i|}\right]^2$$

where $\vec{p}_i$ is the momentum of the $i$-th particle in an event. The unit vector $\vec{n'}$ is defined at minimized $A$.

# C  Comparison

## C.1  Performance of Compensating Pb-scintillator Calorimeter

The compensating Pb-scintillator calorimeter ( sandwich type ) is one of the solutions for the JLC calorimeter.  Energy resolutions of calculation [10], simulation [11], and experiment [12] are summarized in Table 11.

| Constitution | EM | HAD | Group and Ref. |
|---|---|---|---|
| Pb10mm/scinti2.5mm(cal) | - | $40\%/\sqrt{E}$ | R. Wigmans [10] |
| Pb4mm/scinti1mm(sim) | $14\%/\sqrt{E}$ | $52\%/\sqrt{E}$ | Y. Fujii [11] |
| Pb8mm/scinti2mm(sim) | $20\%/\sqrt{E}$ | $53\%/\sqrt{E}$ | Y. Fujii [11] |
| Pb10mm/scinti2.5mm(exp) | $23\%/\sqrt{E}$ | $44\%/\sqrt{E}$ | ZEUS test [12] |

Table 11: *The performance of the compensating Pb-scintillator calorimeter.*

## C.2   Performance of Pb-scintillator Fiber Calorimeter

The compensating Pb-scintillator fiber calorimeter is one of the other solutions for the JLC calorimeter. It is already denoted in the text ( see section 3.1 ) that this type of calorimeter has superior performances than sandwich type. The Pb-scintillator fiber calorimeter has the following merits in general.

- good energy resolution due to fine sampling frequency

- if the calorimeter is compensating, further good energy resolution for hadronic shower

- good position resolution for electromagnetic shower because the fine read-out cross section can be achieved by using the fibers

- small dead space because the photoelectrons are led to the rear of detector by the scintillating fibers

- small detector due to using the lead(Pb) absorber

Experimentally, those excellent performance have been reported by several groups [14] ~ [27] and they are summarized in Table 12.

| Constitution | EM | HAD | POSITION | Group and Ref. |
|---|---|---|---|---|
| Pb/scinti=4/1, 1mm$\phi$ | 13%/$\sqrt{E}$ | 30%/$\sqrt{E}$ | 17mm/$\sqrt{E}$(49 cm$^2$) | SPACAL collab. [14] |
| Pb/scinti=4/1, 0.5mm$\phi$ | 9.2%/$\sqrt{E}$ | - | 2mm/$\sqrt{E}$(4×4 cm$^2$) | RD1 collab. [22] |
| Pb/scinti=1.8/1, 1mm$\phi$ | 9.7%/$\sqrt{E}$ | - | 3mm/$\sqrt{E}$(4×4 cm$^2$) | S. Dagoret, *et al.* [21] |

Table 12: *Experimental results of the compensating Pb-scintillator fiber calorimeter.*

# References

[1] JLC Group, KEK Report 92-16,December,1992.

[2] R. Kajikawa, March 1994, The Report of "SOUGOUKENKYU" A, ( This report was written in Japanese ).

[3] Keisuke FUJII, CERN-EP/90-37, KEK Preprint 92-159, December 1992.

[4] CDF Collaboration, FERMILAB-PUB-94/097-E, CDF/PUB/TUP/PUBLIC/2561.

[5] Bob Jacobsen, CERN-PPE/94-97, June 27, 1994.

[6] F. Richard, ICHEP94, Glasgow, July, 1994.

[7] S. Komamiya, Phys. Rev. D38, 2158, 1988.

[8] T. TSUKAMOTO, KEK Preprint 92-34, May 1992.

[9] I. Nakamura, Master's Thesis, Kobe University, March 1995.

[10] R. Wigmans, Nucl. Instr. and Meth. A259 (1987) 389.

[11] Y. Fujii, *The Third Workshop JLC p355,* KEK Proceedings 92-13, December 1992.

[12] E. BERNARDI *et al.*, Nucl. Instr. and Meth. A262 (1987) 229.

[13] Y. Fujii *et al.*, JLC Calorimeter Group, in preparation.

[14] D. Acosta *et al.*, CERN-EP/90-37, 23 march 1990, CERN-LAA-HC-90-004.

[15] The SPACAL Collaboration, CERN/DRDC/90-23, DRDC/P1, 26.07.1990.

[16] D. Acosta *et al.*, CERN-PPE/90-172, 16 November 1990, CERN-LAA-HC-90-08.

[17] D. Acosta *et al.*, CERN-PPE/91-11, 18 January 1990.

[18] D. Acosta *et al.*, CERN-PPE/91-223, 29 November 1990.

[19] D. Acosta *et al.*, CERN-PPE/92-52, 20 March 1990.

[20] R. Wigmans, Nucl. Instr. and Meth. A315 (1992) 299.

[21] S. Dagoret *et al.*, CERN-PPE/93-147, 12 July 1993.

[22] J. Badier *et al.*, The RD1 Collaboration, CERN-PPE/93-20, 13 January 1993.

[23] J. Badier *et al.*, The RD1 Collaboration, CERN-PPE/93-21, 13 January 1993.

[24] M. Livan, The RD1 Collaboration, CERN-PPE/93-22, 3 February 1993.

[25] A. Asmone *et al.*, CERN-PPE/92-67, 4 March 1990.

[26] G. De Zorzi *et al.*, Nucl. Instr. and Meth. A315 (1992) 327.

[27] K. F. Johnason *et al.*, Nucl. Instr. and Meth. A317 (1992) 506.

[28] Y. Fujii *et al.*, in preparation.

[29] J. Janoth *et al.*, Nucl. Instr. and Meth. A350 (1994) 221.

[30] H2611SXA(24) technical data, Hamamatu Photonics Inc., 314-5, Shimokanzo, Toyooka-village, Iwata-gun, Shizuoka-ken, 438-01 Japan.

[31] R. DeSalvo *et al.*, CERN-LAA-HC/91-006, 15th May 1991, CERN-PPE/91-142, 15th May 1991.

[32] H. Arnaudon *et al.*, Nucl. Instr. and Meth. A342 (1994) 558.

[33] PP350B technical data, Delft Electronische Production, Dwazziewegen 2, Roden, Postbus 60, 9300 AB Roden, the Netherlands.

[34] R. Vaininbroukx and I. Stanef, Nucl. Instr. and Meth. 112 (1973) 111.

[35] 748-73-75-631 technical data, Advanced Photonix Inc., 1240 Avenida, Acaso, Camarillo, CA93012, U.S.A.

[36] P. Cushman and R. Rusack, Nucl. Instr. and Meth. A333 (1993) 381.

[37] T. Hasegawa *et al.*, IEEE trans. on Magnets MAG-28 (1992) 805.

[38] NLPB500, Nichika Chemical Industries, LTD., 491 Oka Kaminaka-cho, Ana-shi, Tokushima-ken, 744 Japan.

[39] B. R. MARTIN and G. SHAW, *Particle Physics,*
John Wiley & Sons Ltd. , Baffins Lane, Chichester West Sussex PO19 1UD, England.

[40] K. Kleinknecht, *PARTICLE DETECTORS,*
It is printed in the EXPERIMENTAL TECHNIQUES IN HIGH-ENERGY NUCLEAR AND PARTICLE PHYSICS *Second Edition,* Edited by Thomas Ferbel, World Scientific Publishing Co. Pte. Ltd. , 73 Lynton Mead, Totteridge, London N20 8DH.

[41] H. Hayashii, *The Second Workshop JLC p360,*
KEK Proceedings 91-10, November 1991.

[42] S. Suzuki, *The Second Workshop JLC p381,*
KEK Proceedings 91-10, November 1991.

Figure 1: *Thrust distributions for $t\bar{t}$ signal and $W^+W^-$ background with all but the thrust cut indicated by an arrow. ( This figure is quoted from Ref.[3]. )*

Figure 2: *(a) An example of energy scan to determine* $m_t$ *and* $\alpha_s(m_Z)$ *where each point corresponds to 1 fb*$^{-1}$*. (b) The contour resulting from the fit to data points. ( This figure is quoted from Ref.[3]. )*

Figure 3: *(a) The reconstructed top momentum distribution at the $t\bar{t}$ threshold, compared with the theoretical expectations for $m_t$ = 150 GeV and $\alpha_s(m_Z)$ = 0.11, 0.12, and 0.13. The Monte Carlo events were generated with $\alpha_s(m_Z)$ = 0.12 and plotted with no acceptance correction. (b) The momentum peak position as a function of $\alpha_s(m_Z)$. The dotted lines indicate the 1-$\sigma$ bounds expected for an integrated luminosity of 100 fb$^{-1}$. ( This figure is quoted from Ref.[3]. )*

Figure 4: *Typical $e^+e^- \to h^0 Z^0$ events with $m_{h^0}$ = 120 GeV; (a) $h^0 \to b\bar{b}$ and $Z^0 \to \nu\bar{\nu}$, (b) $h^0 \to b\bar{b}$ and $Z^0 \to e\bar{e}$, (c) $h^0 \to b\bar{b}$ and $Z^0 \to q\bar{q}$. In pictures (a) to (c), the solid curves represent tracks of the charged particles in the central tracking chamber with a magnetic field of 2.0 Tesla and active radius of 0.3 to 2.3 m, while the dotted lines show photon emissions. The surrounding boxes are electromagnetic clusters, and the lengths of the boxes correspond to their energies. ( This figure is quoted from Ref.[2]. )*

41
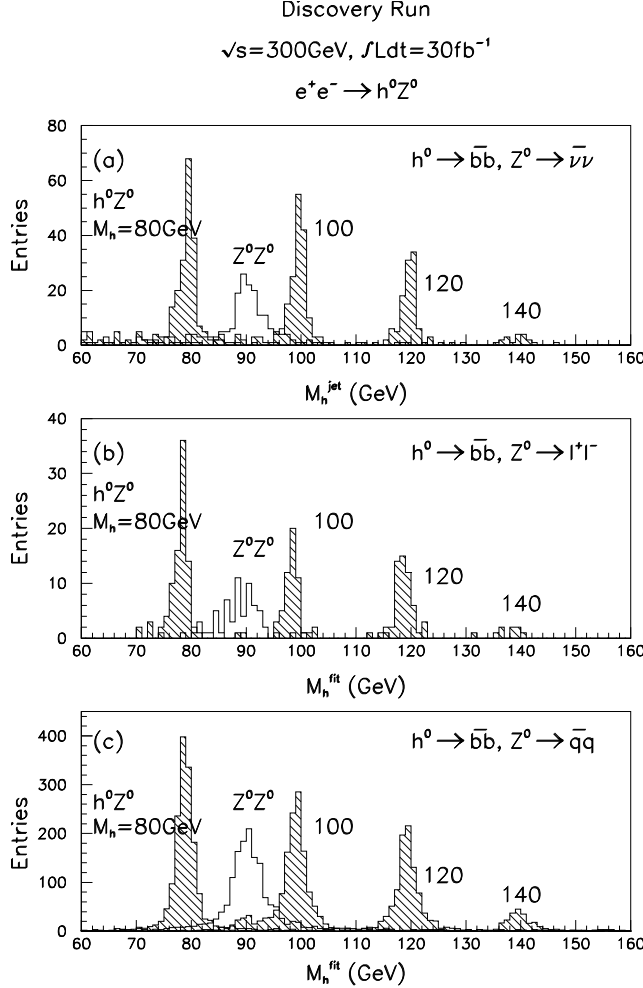
Figure 5: *The reconstructed mass distributions for the three decay channels with an integrated luminosity of 30 fb$^{-1}$. (a) The $m_h^{jet}$ distribution for the decay channel $h^0 \to b\bar{b}$ and $Z^0 \to \nu\bar{\nu}$. (b) The $m_h^{jet}$ distribution for the decay channel $h^0 \to b\bar{b}$ and $Z^0 \to l^+l^-$. (c) The $m_h^{jet}$ distribution for the decay channel $h^0 \to b\bar{b}$ and $Z^0 \to q\bar{q}$. In the figures, the hatched histograms are for the signal process $e^+e^- \to h^0Z^0$ with $m_{h^0}$ = 80, 100, 120, and 140 GeV. The blank histograms are for the background process $e^+e^- \to Z^0Z^0$. ( This figure is quoted from Ref.[2]. )*

Figure 6: *The contour of the total width of* $h^0$. *In this calculation,* $m_t$ *= 150 GeV,* $m_{SUSY}$ *= 1 TeV, therefore,* $m_h$ *< 120 GeV. The total width of the Standard Model Higgs (* $m_{H_{SM}}$ *) for this region is a few MeV at maximum. ( This figure is quoted from Ref.[2]. )*
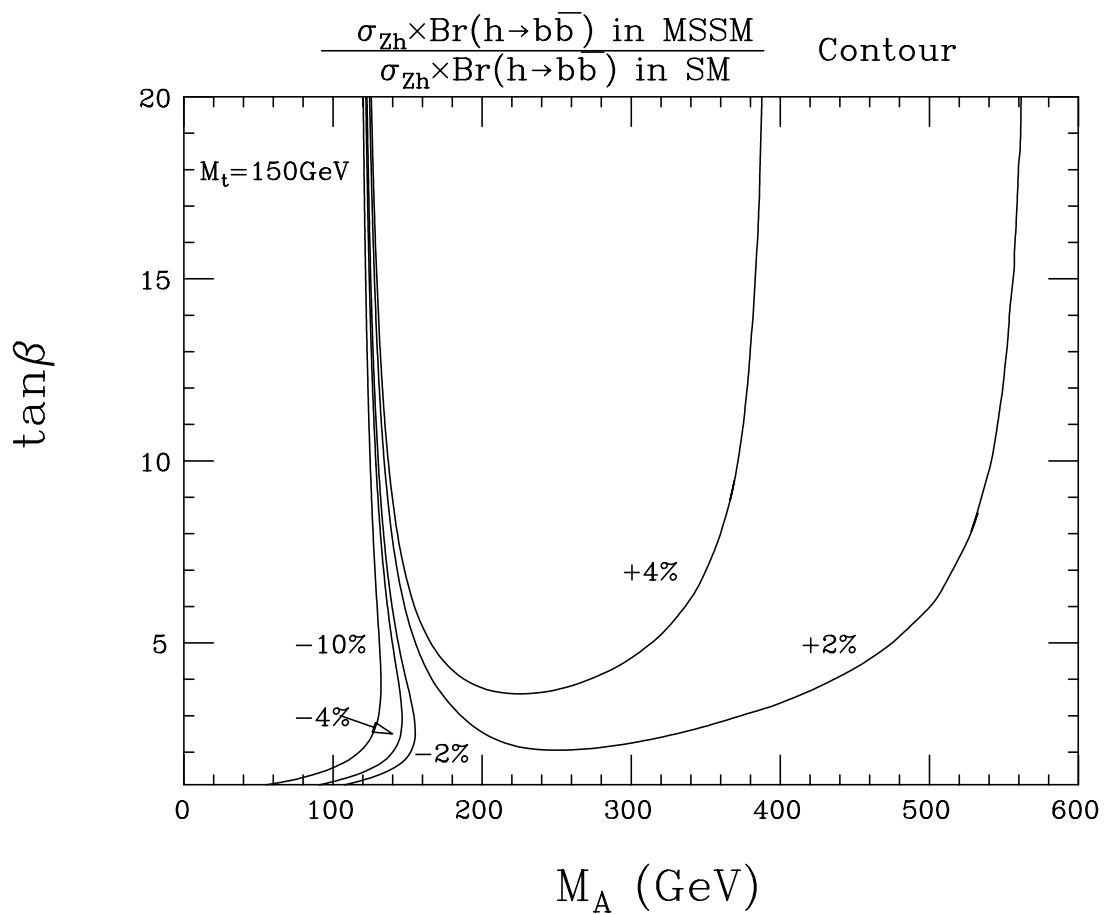
Figure 7: $\sigma_{Zh} \times Br(h^0 \rightarrow b\bar{b})$ in the MSSM compared with that of the Standard Model. ( This figure is quoted from Ref.[2]. )

Figure 8: *The contour of $Br(h^0 \to \tau\bar{\tau})$ in the $\alpha_s$ and $m_b$ plane. The parameters of the Higgs boson are adjusted to obtain $m_h$ = 100 GeV. ( This figure is quoted from Ref.[2]. )*

Figure 9: *An example of the acoplanarity distribution for the 2-jets + 1 lepton final states from the lighter chargino pair productions in the case of $m_0$ = 400 GeV, $M_2$ = 400 GeV, $\mu$ = 250 GeV, and tan$\beta$ = +2. The Monte Carlo data correspond to an integrated luminosity of 10 fb$^{-1}$ at $\sqrt{s}$ = 500 GeV. The solid histogram is the chargino pair, while the dashed and dotted histogram are backgrounds from the $W$ pair and $e\nu W$, respectively. ( This figure is quoted from Ref.[2]. )*

Figure 10: *The energy distribution of the 2-jets systems from the lighter chargino decays for Monte Carlo data corresponding to an integrated luminosity of 20 fb$^{-1}$, where the Supersymmetric parameters are the same as with Fig.9. The solid line is the best fit curve, the dashed and dotted line corresponds the expected backgrounds from the $W$ pair and $e\nu W$, respectively. ( This figure is quoted from Ref.[2]. )*

Figure 11: *The energy distribution of the W boson from the lighter chargino decays for Monte Carlo data corresponding to an integrated luminosity of 50 fb$^{-1}$, where the Supersymmetric parameters are $m_0$ = 70 GeV, $M_2$ = 400 GeV, $\mu$ = 250 GeV, and tan$\beta$ = +2. The solid line is the best fit curve, the dashed, dot-dashed, and dotted line corresponds the expected backgrounds from the $W$ pair, $e\nu W$, and the others ( $WWZ, eeWW, \nu\nu WW$ ), respectively. ( This figure is quoted from Ref.[2]. )*

Figure 12: *Reconstructed dijet mass resolution for Higgs boson in the $e^+e^- \rightarrow Z^0h^0$ process. ( This figure is quoted from Ref.[1]. )*
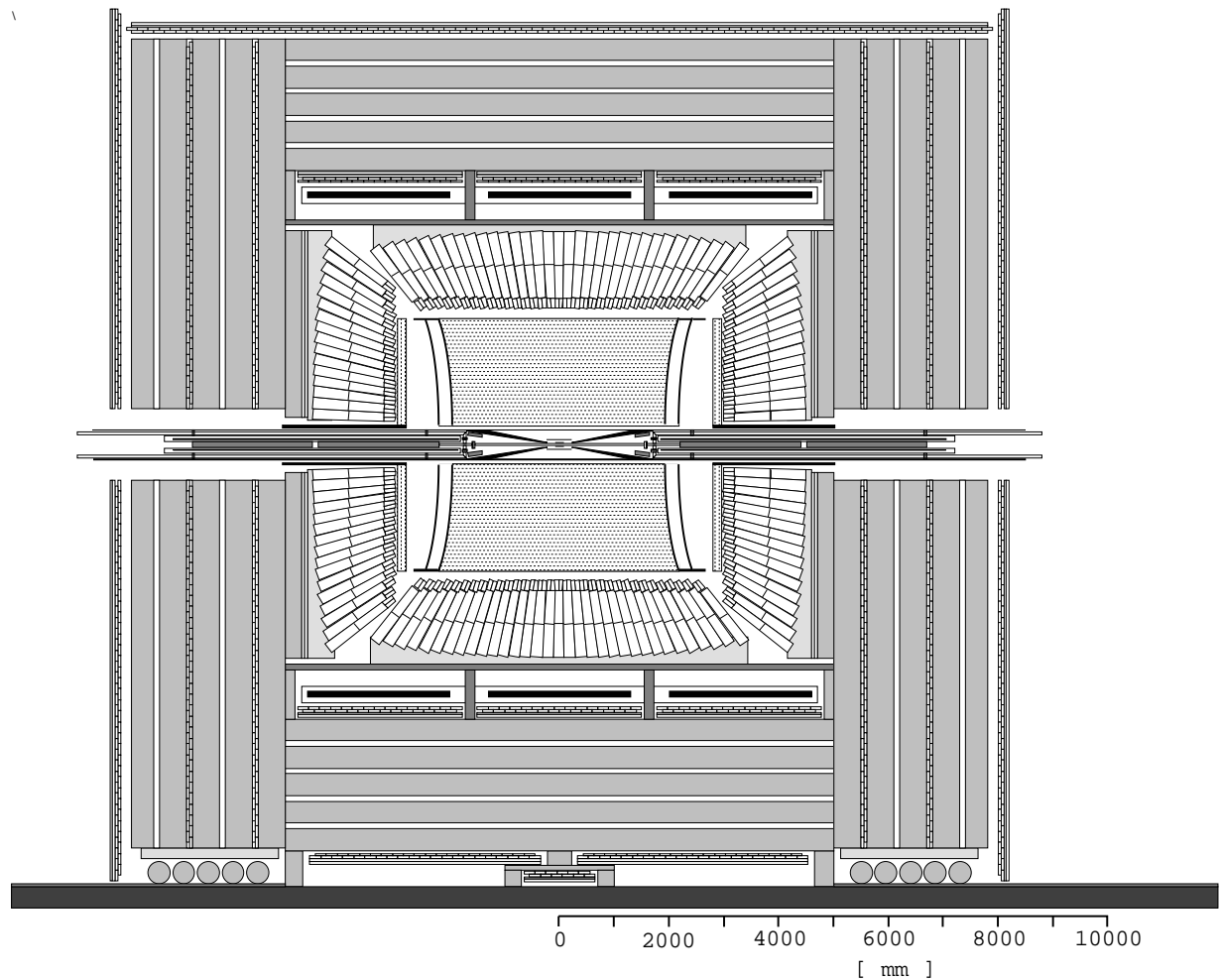
Figure 13: *Schematic drawing of the JLC detector. ( This figure is quoted from Ref.[1]. )*

Figure 14: *Schematic view of Spaghetti calorimeter.*
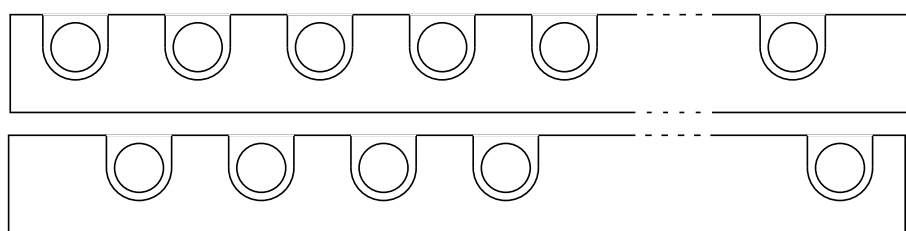


Figure 15: *The cross section of lead plate.*

**STAGE**
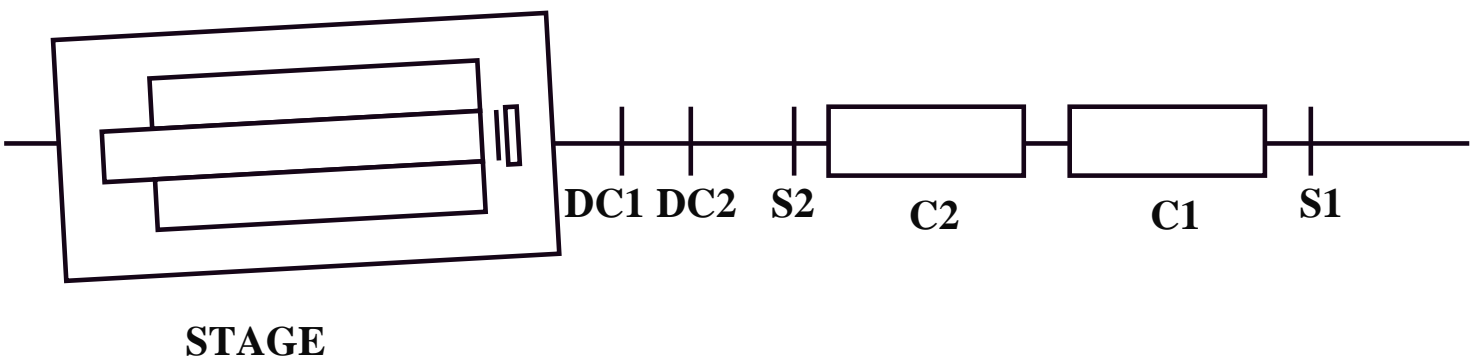
Figure 16: *Setup of the beam test.*



Spaghetti
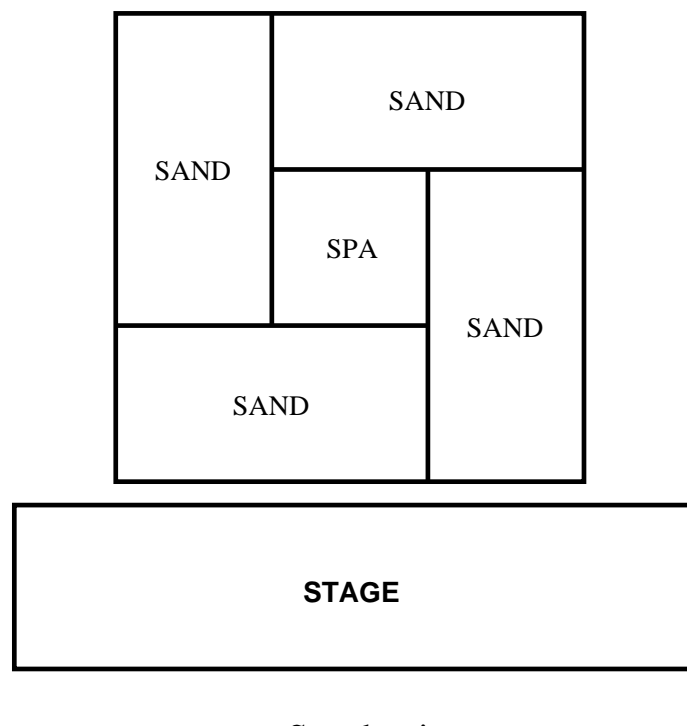
Figure 17: *Arrangement of calorimeters.*
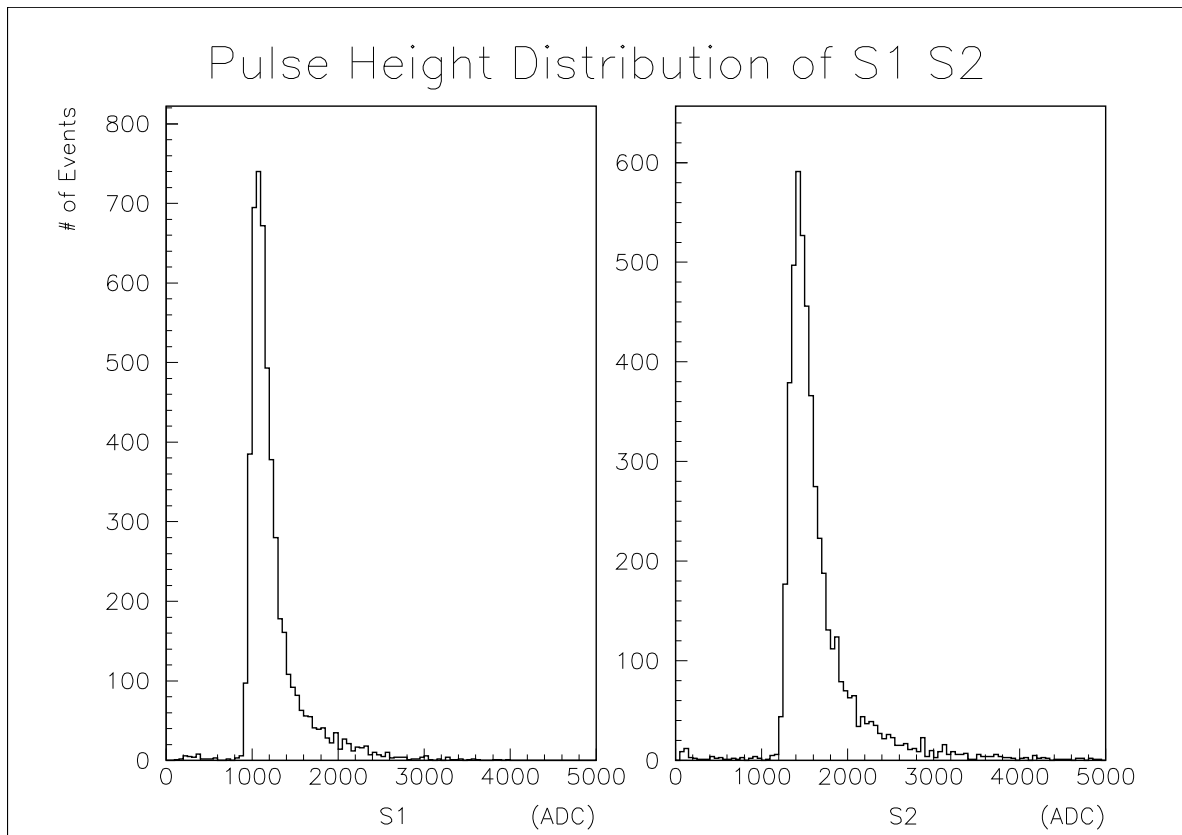
Figure 18: *Typical pulse height distribution of the trigger counters.*
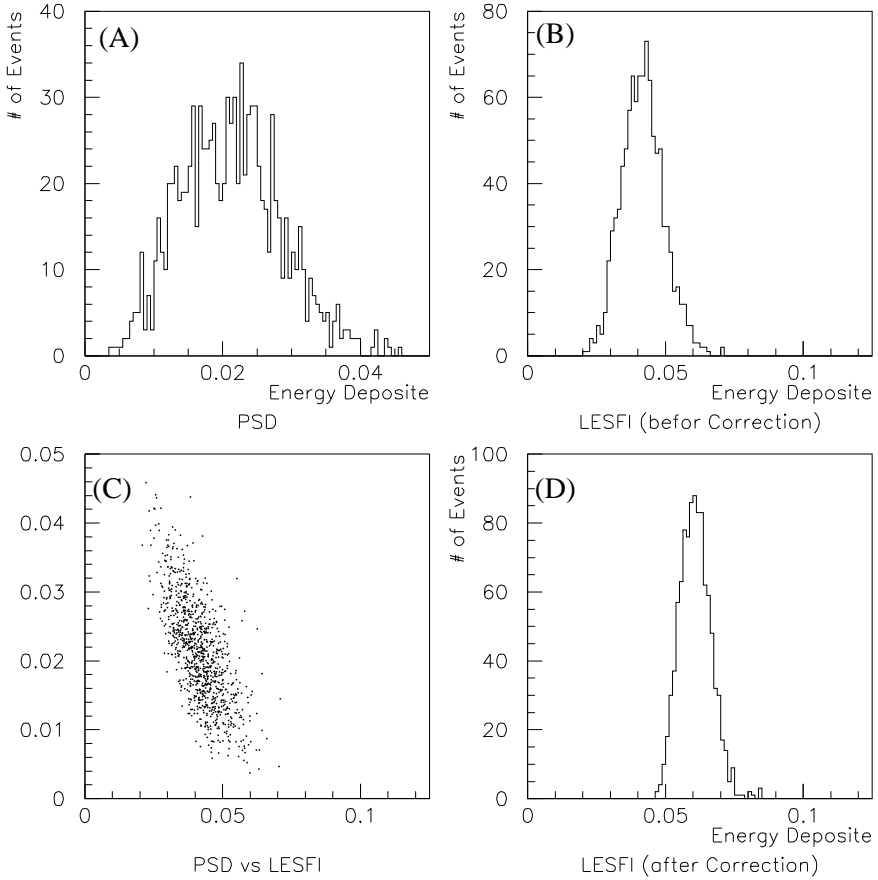
Figure 19: *Total energy distribution for 2.5GeV electrons at $\theta_x = 3°$ with the PSD. The correction of the $E_{PSD}$ is applied. (A) The signal distribution of the PSD. (B) The total energy distribution of test modules before correction. (C) The scatter plot of PSD versus LEAD/SCIFI . (D) The total energy distribution of test modules after correction. The energy resolution ( $\sigma_E/E = 9.45 \pm 0.50\%$ is obtained by gaussian fit.*
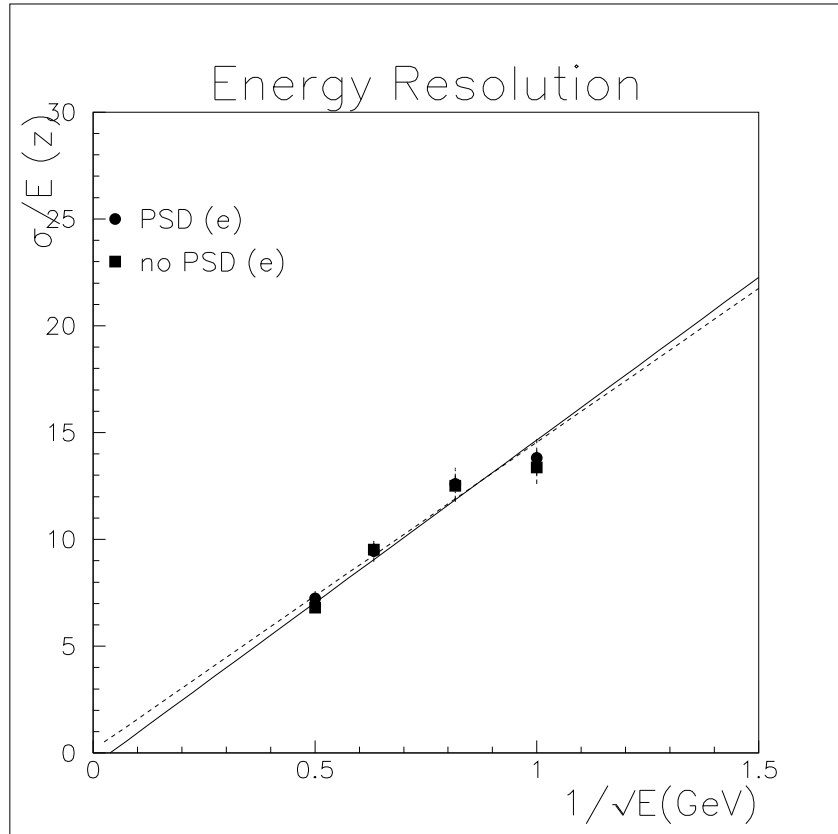
Figure 20: *Energy resolution for electrons of* $\theta_x = 3°$, *as a function of the* $\sqrt{E}^{-1/2}$. *The solid line represent the resulting of linear fit to the data without PSD, and dashed line represent one with PSD.*
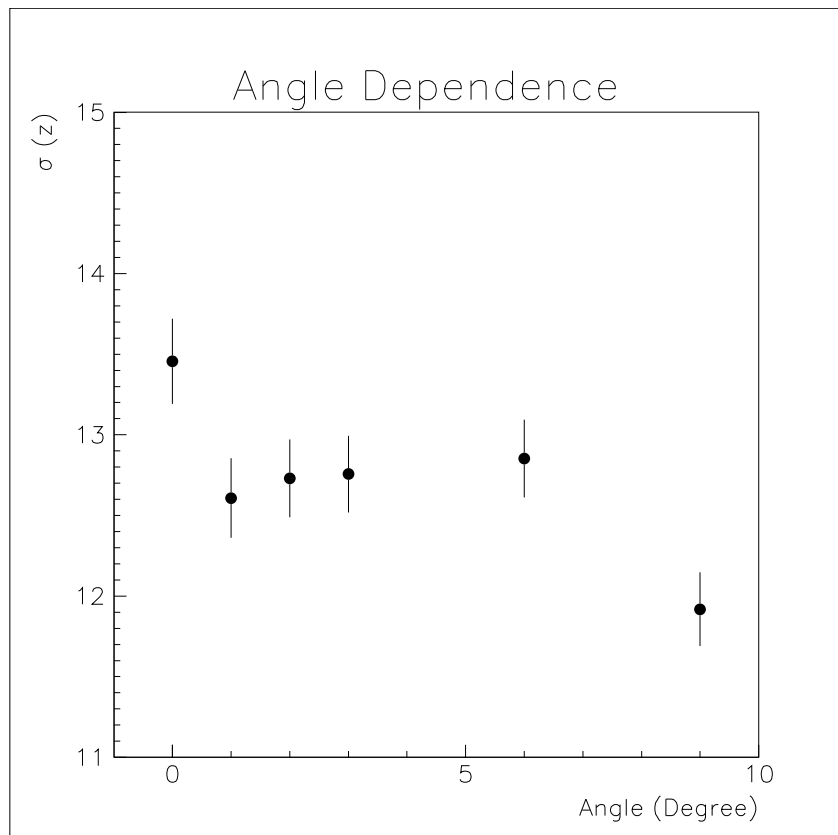
Figure 21: *Energy resolution of electrons for 2.5 GeV without PSD, as a function of the incident angle $\theta_x$.*
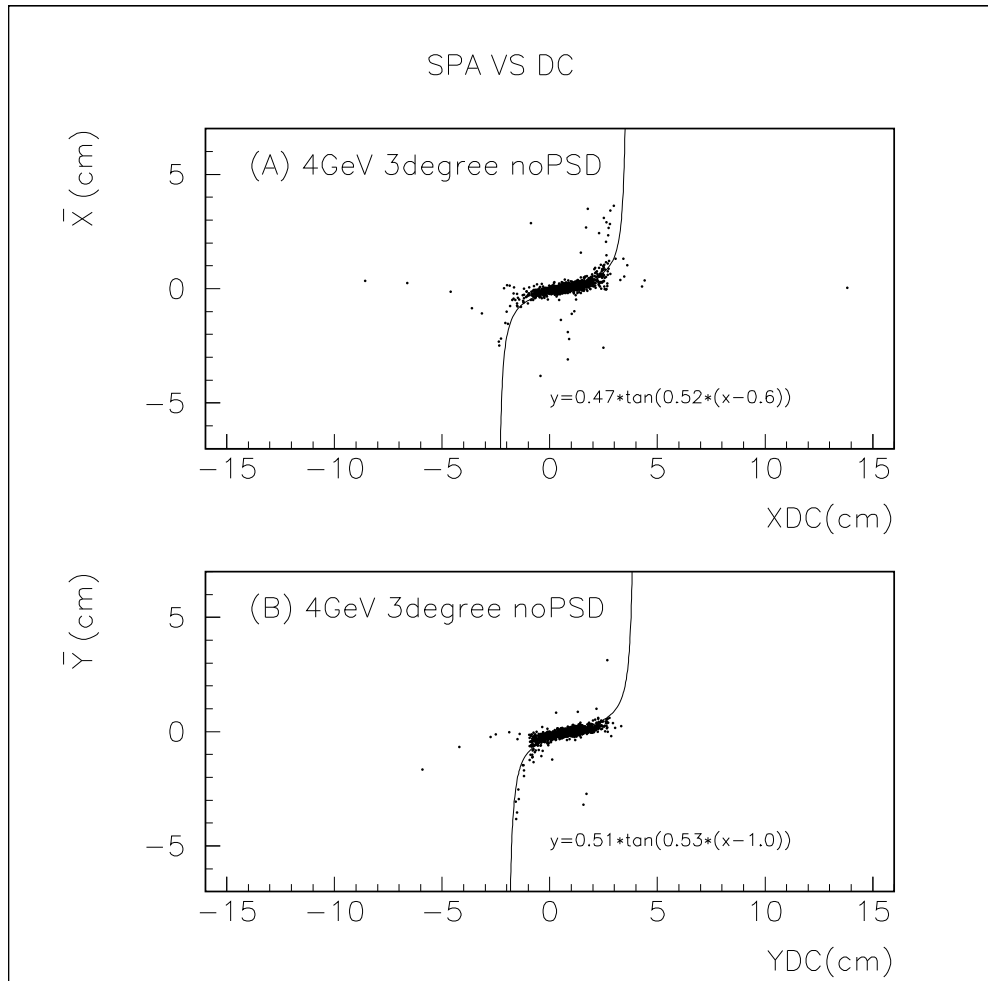
Figure 22: *Scatter plot for 4 GeV electrons, showing the position from DC 's data versus from LEAD/SCIFI 's data. (A) x-coordinate, (B) y-coordinate. We use the data taken without PSD at $\theta_x = 3°$. The solid line is the result from fitting with the tangent function.*
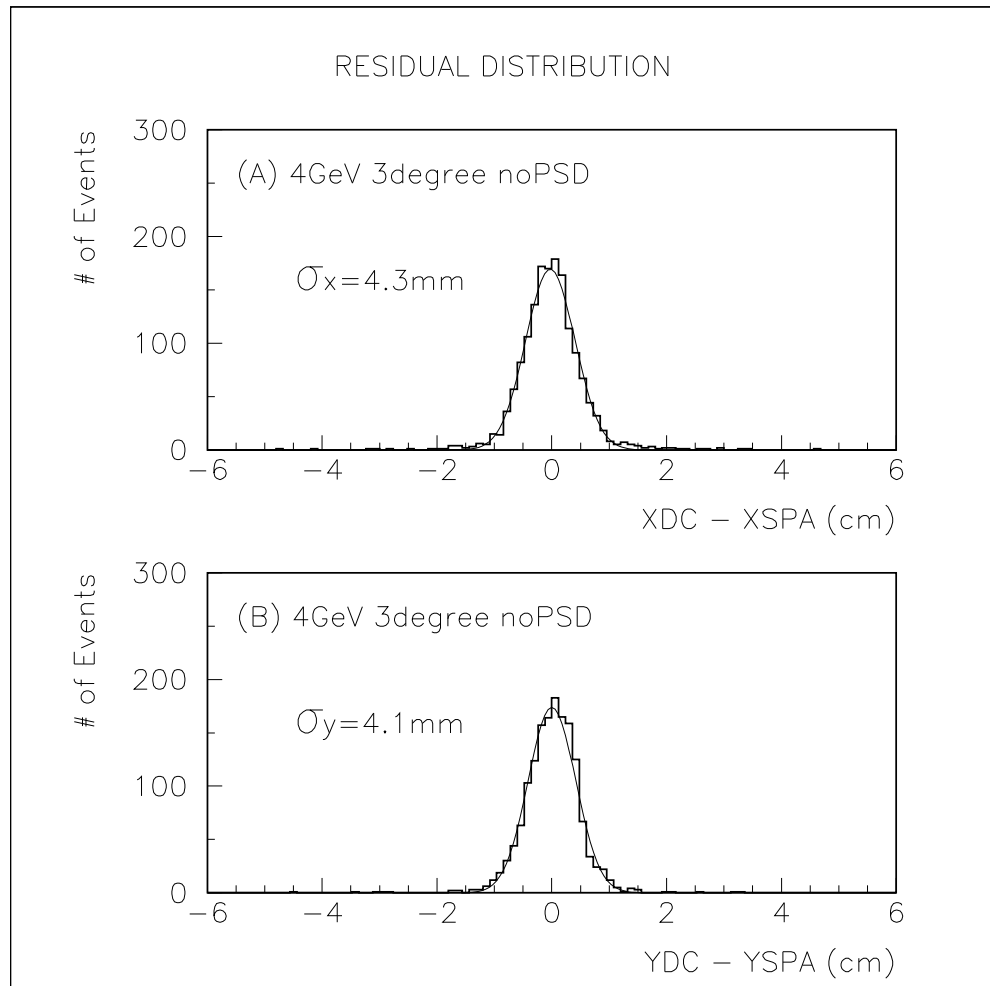
Figure 23: *Residual distribution for electrons of 4 GeV. (A) x-coordinate, (B) y-coordinate. We use the data taken without PSD at $\theta_x = 3°$. The result from gaussian fit is also figured.*
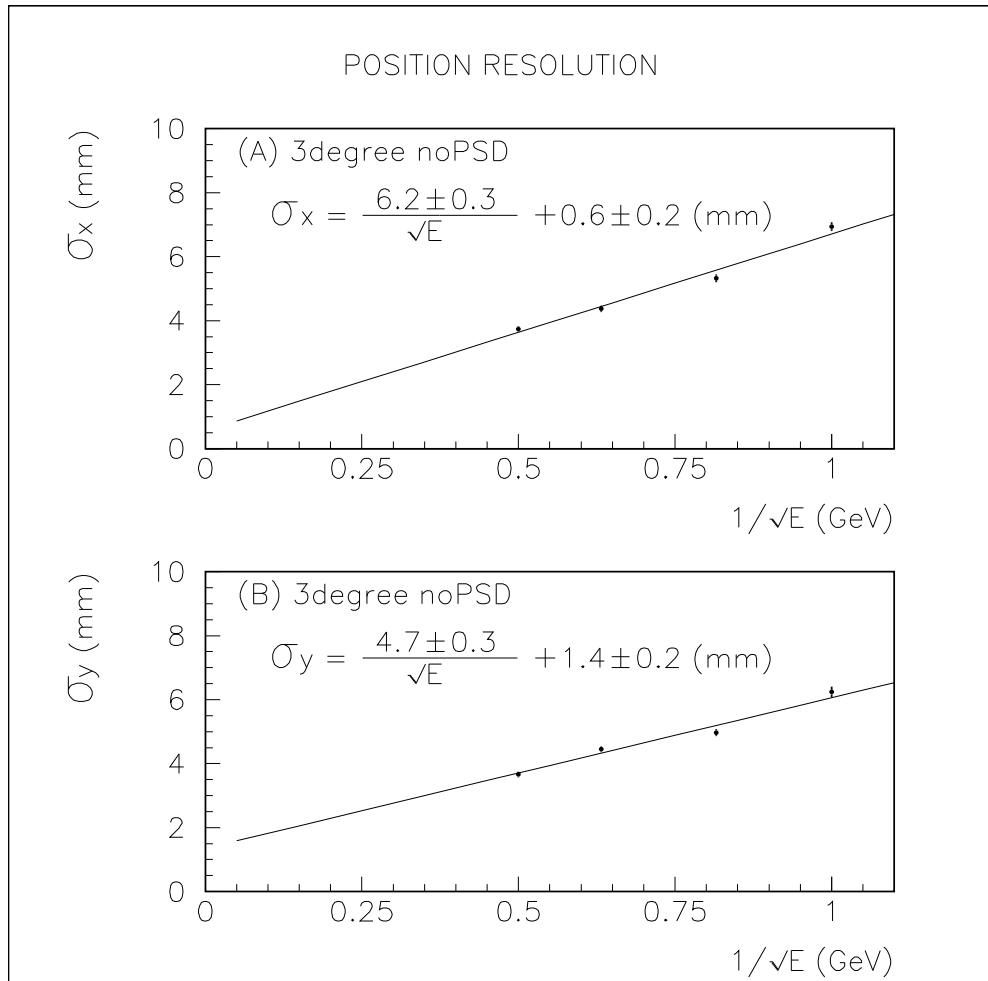
Figure 24: *Position resolution for electrons as a function of the $\sqrt{E}^{-1/2}$. (A) x direction, (B) y direction. We use the data taken without PSD at $\theta_x = 3°$. The solid line is the result from linear fit.*
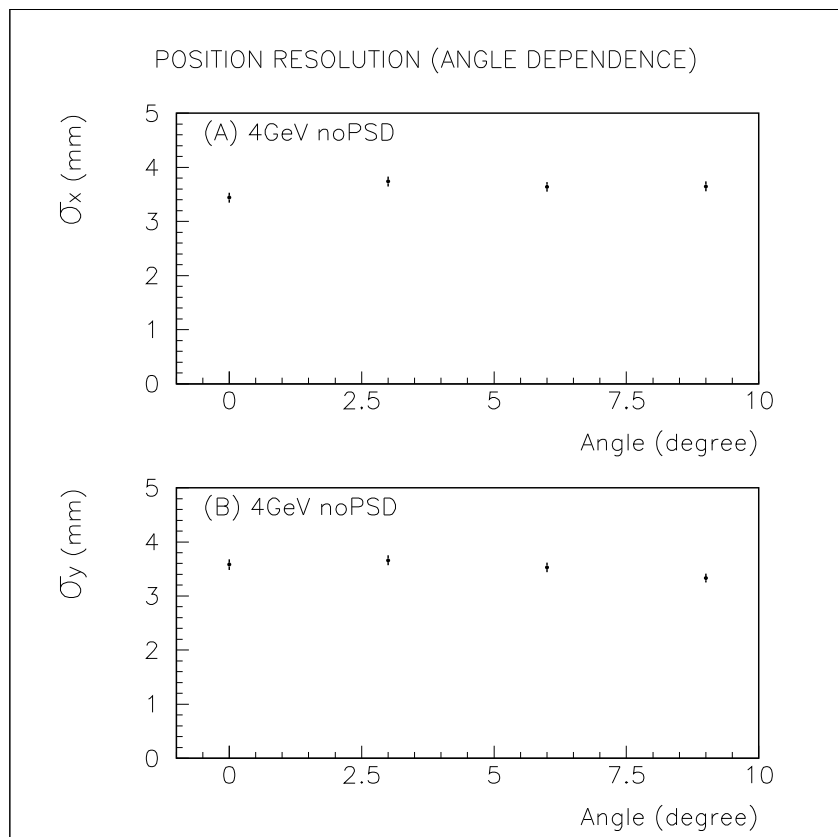
Figure 25: *Position resolution of electrons for 4.0 GeV without PSD, as a function of the angle* $\theta_x$.
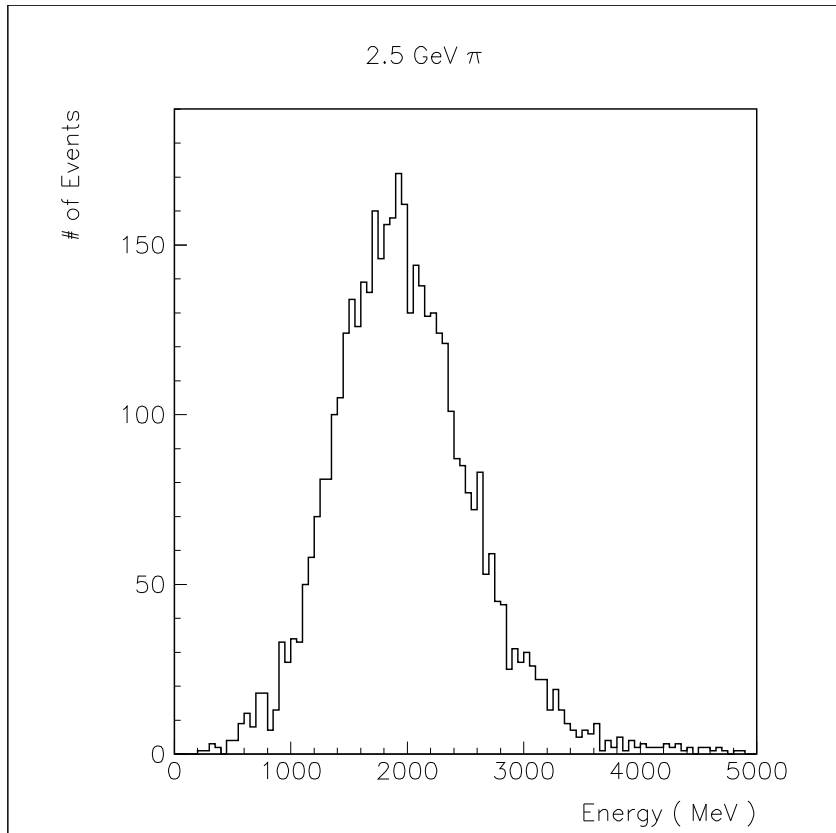
Figure 26: *Total energy distribution for 2.5GeV pions at $\theta_x = 0°$ with the PSD. The energy is normalized by electron shower. The energy resolution ( $\sigma_E/E = 28.63 \pm 0.48\%$ is obtained by gaussian fit.*
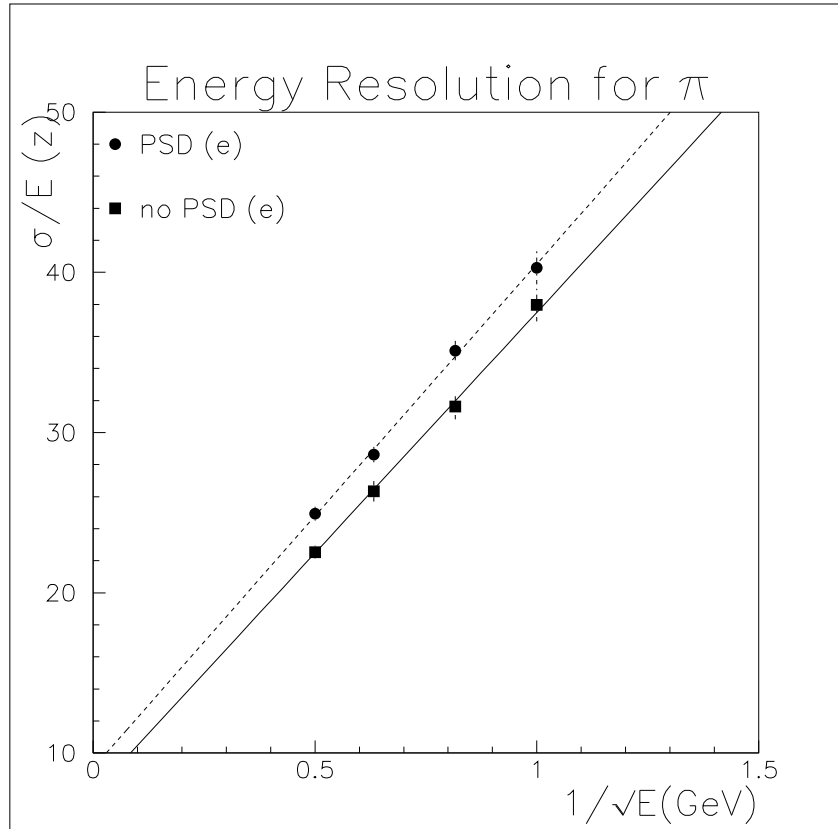
Figure 27: *Energy resolution for pions of $\theta_x = 0°$, as a function of the $\sqrt{E^{-1/2}}$. The solid line represent the resulting of linear fit to the data without PSD, and dashed line represent one with PSD.*
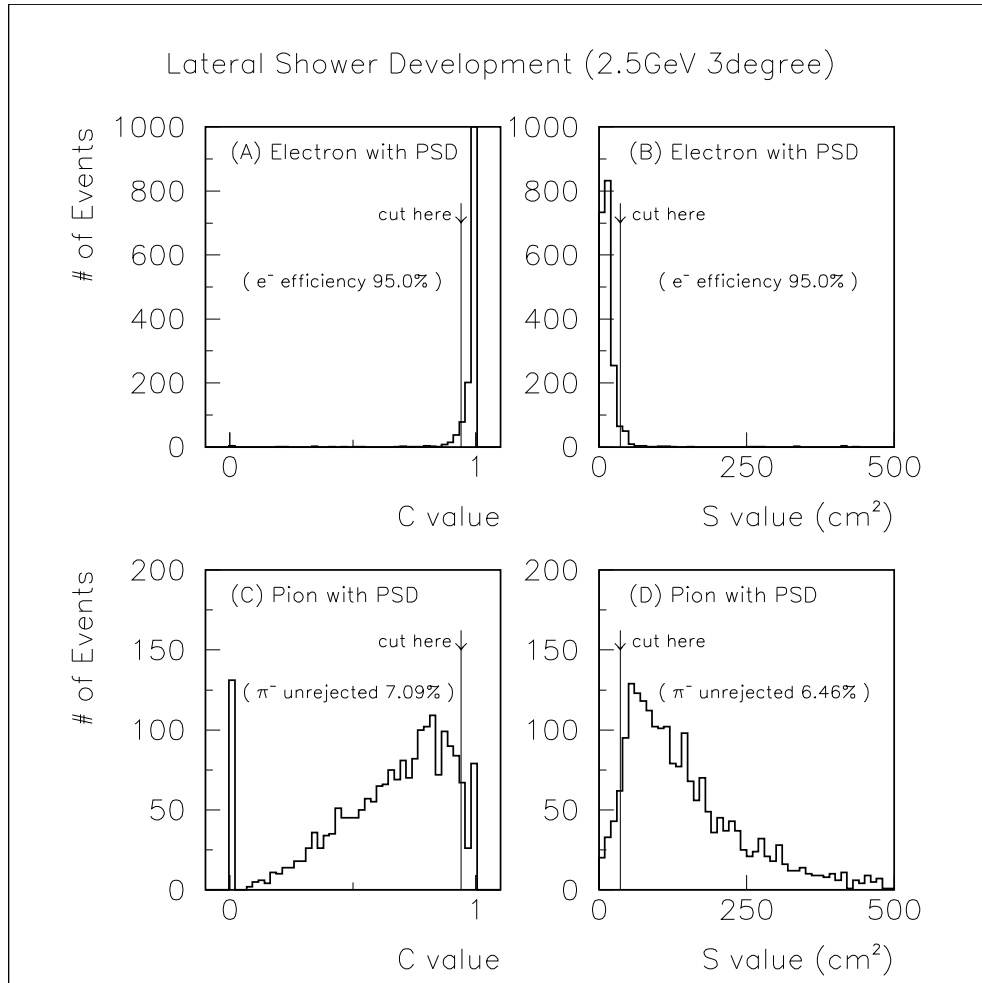
Figure 28: *Distribution of the lateral shower spread. (A) $C$ value for electrons of 2.5 GeV. (B) $S$ value for electrons of 2.5 GeV. (C) $C$ value for pions of 2.5 GeV. (D) $S$ value for pions of 2.5 GeV. The cut of >0.94 for $C$ value gives the 95% electron efficiency and the 14.1 pion rejection factor. The cut of <36.5 for $S$ value gives the 95% electron efficiency and the 15.5 pion rejection factor.*
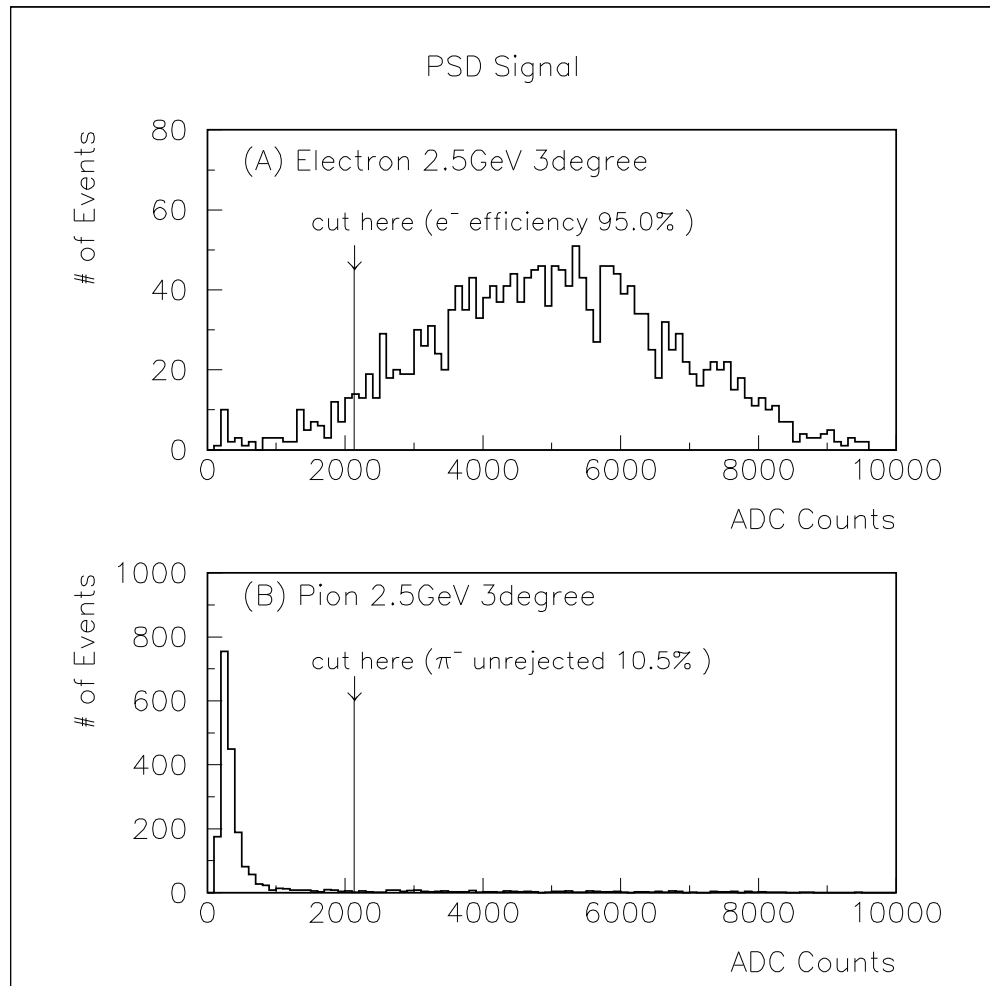
Figure 29: *The pulse height distribution of PSD. (A) 2.5 GeV Electrons, (B) Pions. The cut of >2130 gives the 95% electron efficiency and the 9.56 pion rejection factor.*

Figure 30: *Scatter plot of PSD siganl versus C value. The circle represents the electron data, the open square represents the pion one. We use the data taken at $\theta_x = 0°$ and 2.5 GeV beam energy. The cut of PSD>1900 and C>0.9 give the 95% electron efficiency and the 74.1 pion rejection factor.*
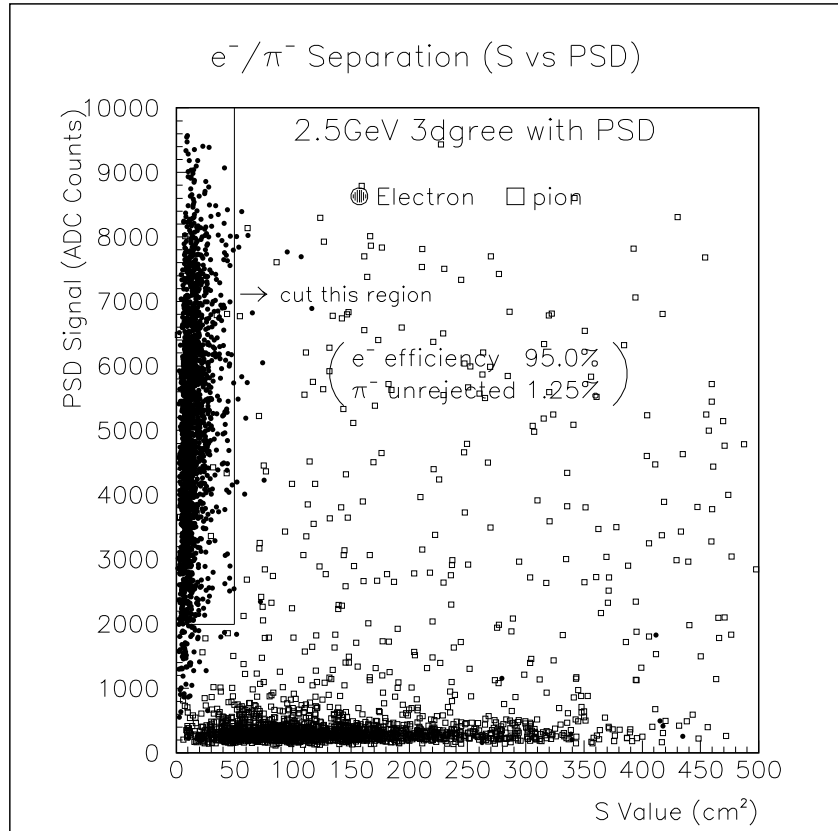
Figure 31: *Scatter plot of PSD siganl versus S value. The circle represents the electron data, the open square represents the pion one. We use the data taken at $\theta_x = 0°$ and 2.5 GeV beam energy. The cut of PSD>1995 and S<50 give the 95% electron efficiency and the 79.8 pion rejection factor.*
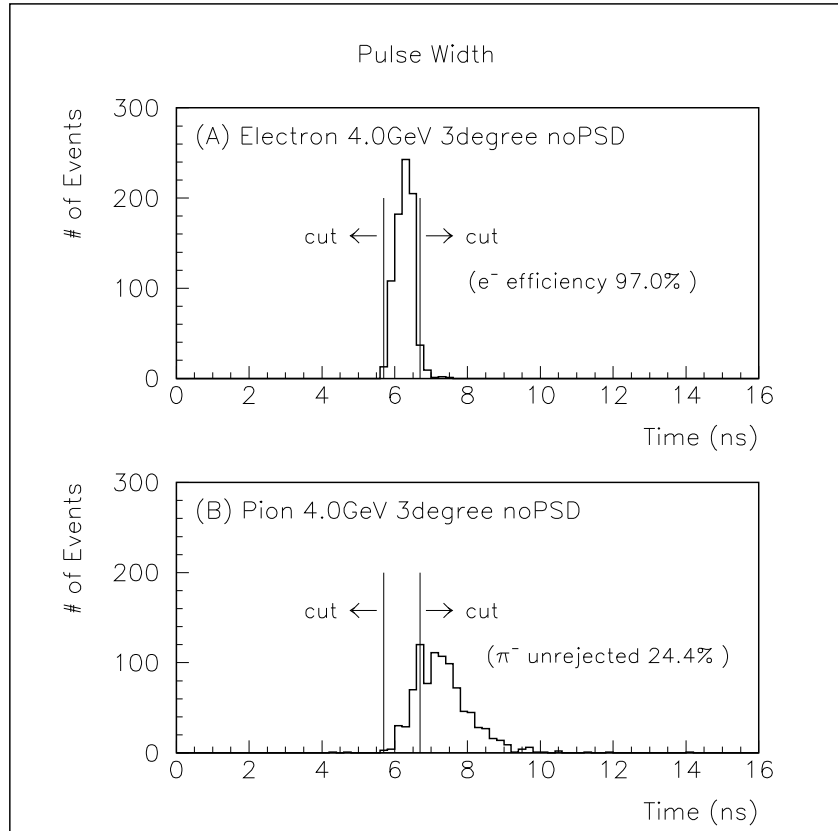
Figure 32: *The distributions of the pulse widths ( PWD ) with the test module. The data was taken with the digital oscilloscope of 2GHz sampling. (A) 4.0 GeV electrons, (B) 4.0 GeV pions. The incident position and angle were the center of the segment and 3° in the horizontal plane. The cut of 5.7 < PWD < 6.7 give the 97% electron efficiency, and the 4.1 pion rejection factor.*
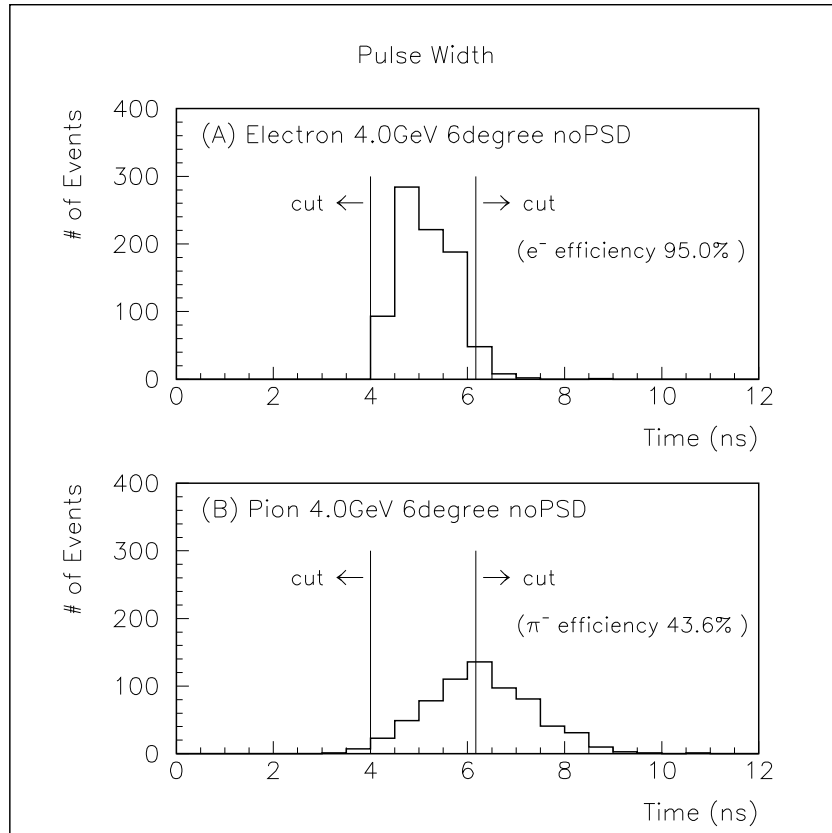
Figure 33: *The distributions of the pulse widths ( PWD ) with the special test module. The data was taken with the digital oscilloscope of 2GHz sampling. (A) 4.0 GeV electrons, (B) 4.0 GeV pions. The incident position and angle were the edge of the segment and 6° in the horizontal plane. The cut of 4 < PWD < 6.17 give the 95% electron efficiency, and the 2.29 pion rejection factor.*
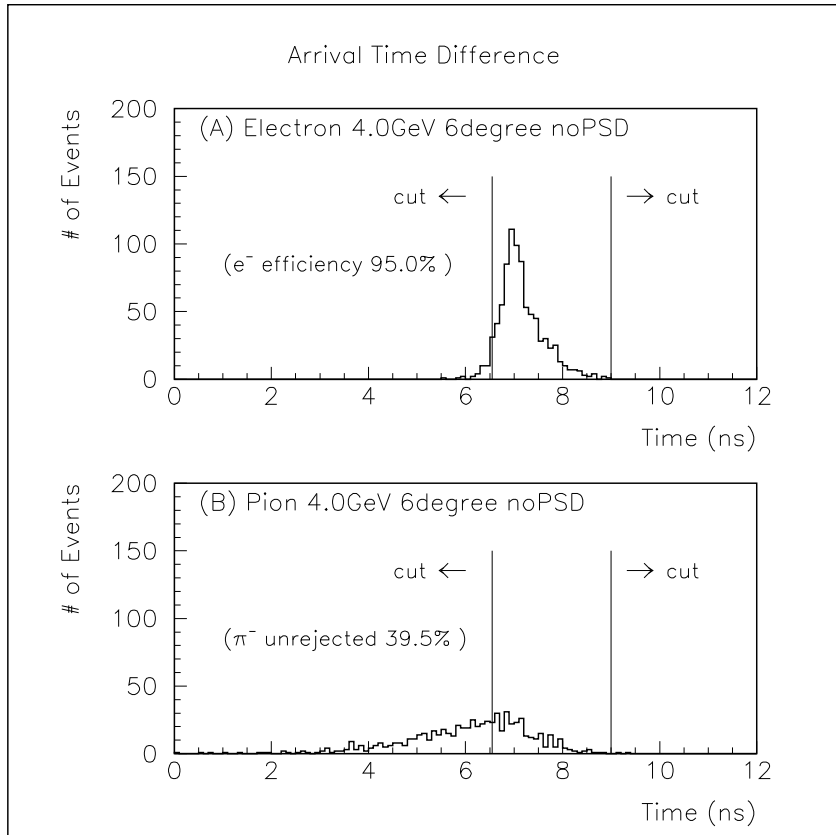
Figure 34: *The distributions of the timing differences ( TD ) of the signals at both ends. We use the special test module and the data was taken with the digital oscilloscope of 2GHz sampling. (A) 4.0 GeV electrons, (B) 4.0 GeV pions. The incident position and angle were the edge of the segment and 6° in the horizontal plane. The cut of 6.55 < TD < 9.0 give the 95% electron efficiency, and the 2.53 pion rejection factor.*
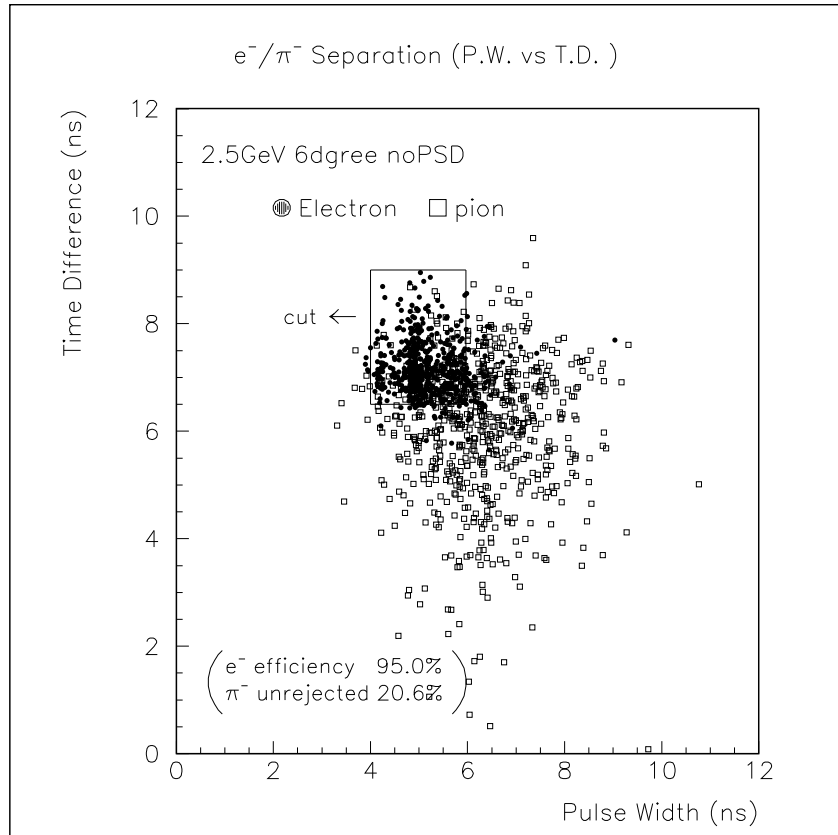
Figure 35: *The scatter plot of the pulse widths ( PWD ) and timing differences ( TD ). We use the data incident to the special test module, taken with the digital oscilloscope of 2GHz sampling at the 4.0 GeV beam energy. The incident position and angle were the edge of the segment and 6° in the horizontal plane. The cut of 4 < PWD < 6.43 and 6.5 < TD < 9.0 give the 95% electron efficiency, and the 4.85 pion rejection factor.*

70

Figure 36: *Configuration of FMPMT.*

Figure 37: *Configuration of HPD.*

Figure 38: *Configuration of VAPD.*

Figure 39: *Schematic view of the test setup.*

Figure 40: *The distribution of the LED light on the photocathode.*

Figure 41: *Dependence of the LED light yield on the magnetic field strength.*

Figure 42: *Uniformity of FMPMT.*

Figure 43: *Uniformity of HPD.*

Figure 44: *Dependence of the FMPMT gain on the magnetic field strength. The data are normalized at -2.7 kV high voltage.*

Figure 45: *Dependence of the FMPMT gain on the tilt angle. The data are also normalized at -2.7kV high voltage.*

Figure 46: *Dependence of the HPD gain on the magnetic field strength.*

Figure 47: *Dependence of the HPD gain on the tilt angle.*

Figure 48: *Dependence of the VAPD gain on the magnetic field strength.*

Figure 49: *Dependence of the VAPD gain on the tilt angle.*